INFRARED SPECTROSCOPY OF ZINC OXIDE AND MAGNESIUM NANOSTRUCTURES

By

WIN MAW HLAING OO

A dissertation submitted in partial fulfillment of
the requirements for the degree of

DOCTOR OF PHILOSOPHY

WASHINGTON STATE UNIVERSITY
Materials Science Program

DECEMBER 2007

To the Faculty of Washington State University:

The members of the Committee appointed to examine the dissertation of WIN MAW HLAING OO find it satisfactory and recommend that it be accepted.

Chair

ACKNOWLEDGEMENTS

Many people have helped me accomplish this dissertation, and I owe my gratitude to all of them.

First and foremost I would like to thank my advisor, Prof. Matthew McCluskey, without whose guidance and advice this dissertation would not be what it is today. His patience and support rescued me from despair on countless occasions. I am also thankful to Prof. Susan Dexheimer and Prof. Grant Norton for serving on my dissertation committee and for their invaluable suggestions and help.

I wish to express my gratitude to former members of McCluskey group; Dr. Slade Jokela and Dr. Kirill Zhuravlev for offering their expertise. I am also grateful to Gabriel Hanna, Marianne Tarun, Jennie Schei and Bobbie Riley who are current members for their help.

I would like to thank the members of Departments of Physics and Astronomy, and Materials Science Program. Thanks to all of my friends, especially Natnael Embaye, Francis Morrissey, Christopher Dudley, Jalal Nawash, and Loren Cramer for their encouragement.

I am also grateful to Prof. Leah Bergman (University of Idaho) and Prof. Yiping Zhao (University of Georgia), as well as their research group members for their collaborations.

The Summer Research Institute at Pacific Northwest National Laboratory (PNNL) provided me an opportunity to conduct a research project during the summer of 2007. I wish to extend my warm thanks to Dr. Laxmikant Saraf and other staff members of

Environmental Molecular Sciences Laboratory at PNNL.

Despite all the support and help I have received, I am solely responsible for any mistakes herein.

I also wish to express my appreciation to my brother and sister for their thoughtful care and concerns for me.

Last, but certainly not least, my deepest thanks go to my parents for supporting and encouraging me to achieve and be successful. I am forever grateful to them for showing me the value of education.

This work was supported in part by the National Science Foundation under Grant Nos. DMR-0203832, DMR-0704163, and Department of Energy Hydrogen Initiative Award Nos. DE-FG02-05ER46251, DE-FG02-07ER46356. The American Chemical Society Petroleum Research Fund also provided partial support.

INFRARED SPECTROSCOPY OF ZINC OXIDE AND MAGNESIUM NANOSTRUCTURES

Abstract

by Win Maw Hlaing Oo, Ph.D.
Washington State University
December, 2007

Chair: Matthew D. McCluskey

Impurities in ZnO nanoparticles and Mg nanorods were investigated. ZnO nanoparticles were prepared by a reaction of zinc acetate and sodium hydrogen carbonate. The presence and source of CO_2 impurities in ZnO nanoparticles were studied by infrared (IR) spectroscopy. Isotopic substitution was used to verify the vibrational frequency assignment. Isochronal annealing experiments were performed to study the formation and stability of molecular impurities. The results indicate that the molecules are much more stable than CO_2 adsorbed on bulk ZnO surfaces.

IR reflectance spectra of as-grown and hydrogen-annealed ZnO nanoparticles were measured at near-normal incidence. The as-grown particles were semi-insulating and showed reflectance spectra characteristic of insulating ionic crystals. Samples annealed in hydrogen showed a significant increase in electrical conductivity and free-carrier absorption. A difference was observed in the *reststrahlen* line shape of the conductive sample compared to that of the as-grown sample. The effective medium approximation was applied to model the reflectance and absorption spectra. The agreement between the experimental results and the model suggests that the nanoparticles have inhomogeneous carrier concentrations. Exposure to oxygen for several hours led to a significant decrease in carrier concentration, possibly due to the adsorption of negative oxygen molecules on the nanoparticle surfaces.

Cu doped ZnO nanoparticles were prepared by using a zinc acetate/copper acetate precursor. The electronic transitions of Cu^{2+} ions were observed in the IR absorption spectrum at low temperatures. The high resistivity property of ZnO:Cu nanoparticles was observed.

Magnesium hydroxide thin layers were formed by a chemical reaction between magnesium nanorods and water. IR spectroscopy showed hydroxide (OH) vibrational modes. The assignment was verified by reactions with heavy water which produced the expected OD vibrational frequency. A Fano interference was detected for hydroxide layers formed on metallic magnesium. For hydroxide layers on insulating magnesium hydride, however, the line shape was symmetric and no Fano resonance was observed. The results show that the hydroxide layer is thin such that the vibrational motion couples to the free electron continuum of the magnesium metal.

TABLE OF CONTENTS

LIST OF FIGURES

LIST OF TABLES

CHAPTER 1

INTRODUCTION

Control of the electrical and optical properties of nanoparticles is a key requirement for practical applications in optoelectronic devices. The control of the number of free carriers has been achieved by doping the nanoparticles. Doped semiconductors contain impurities, foreign atoms which are incorporated into the host crystal intentionally or unintentionally. In this work, we investigated impurities in ZnO and Mg nanostructures.

1.1 Semiconductors at the nanometer scale

As particles approach the nanoscale, they possess two important properties, (1) the quantum confinement effect [1] and (2) a large ratio of surface area to volume relative to bulk materials. The large surface area provides numerous atomic sites for the adsorption of molecules, making the nanoparticles attractive materials for gas and chemical sensing. Since nanoparticles are small compared to IR and visible wavelengths, they exhibit characteristic absorption and scattering properties [2]. This feature has been utilized for materials such as stained glass for many centuries.

1.2 Free-carrier concentration

The free-carrier concentration is an important parameter that controls the electrical properties of a semiconductor. Electronic energy levels in a semiconductor crystal are separated by a bandgap energy E_g, which is the minimum energy separation between the conduction band and valence band.

1.2.1 Intrinsic

In a bulk semiconductor, the number of atoms is assumed to be infinite. The intrinsic free-carrier concentration n_i at a given temperature T is given by an Arrhenius equation [3]:

$$n_i = \sqrt{N_v N_c} \exp\left(-\frac{E_g}{2kT}\right), \tag{1.1}$$

where E_g is the bandgap energy and k is Boltzmann's constant. The pre-factors N_v and N_c are the effective density of states of the valence and conduction bands respectively, and are typically expressed in units of cm^{-3}. In an intrinsic semiconductor, there is an equal number of electrons and holes.

1.2.2 Doping

Introducing impurity atoms into a semiconductor host leads to an increase in the free-carrier concentration. In n-type semiconductors, free electrons in the conduction band are majority charge carriers, whereas holes in the valence band are majority carriers in p-type semiconductors. Shallow donors and acceptors have a much smaller ionization energy compared to the bandgap energy of the host semiconductor; hence, they can readily contribute to electrical conductivity.

1.2.3 Free-carrier concentration in semiconductor nanoparticles

In nanoparticles, the number of atoms within a particle is limited ($\sim 10^3 - 10^5$). Thus, in some cases, the particles contain no free carriers. The properties of a particle can be changed dramatically when a single dopant is added to or removed from the particle. Precise control over dopant concentration within each particle is extremely difficult. Bryan and Gamelin [4] proposed that the dopant distribution among the nanoparticles can be described by a binomial expression,

$$P(n|N) = \frac{(N)!}{n!(N-n)!}(xN)^n[1-(xN)]^{N-n}, \tag{1.2}$$

where n is the number of dopants per nanoparticle. The value N is total number of sites available for substitution and x is dopant mole fraction.

1.3 Zinc Oxide (ZnO)

Zinc oxide (ZnO) [5,6] is a wide bandgap (3.4 eV at room temperature) semiconductor that is desirable for many applications. It is attractive for forming various forms of nanostructures, such as nanorods, nanowires, and nanobelts [7]. Alloying with MgO or CdO respectively increases or decreases the bandgap energy of ZnO [8]. Transparent transistors fabricated from ZnO have been reported [9]. With its high exciton binding energy, ZnO is a good candidate for room temperature UV lasers [10]. Its large piezoelectric constant is promising for ultrasonic tranducers [11]. ZnO is transparent and electrically conductive, making it an ideal material for solar cell windows [12]. One of the major commercial applications of ZnO is the production of varistors [13]. ZnO varistors have high non-ohmic voltage-current characteristics, which originate from grain boundaries between ZnO grains. The mineral form of ZnO can be found in nature and is known as Zincite.

Zinc oxide has the hexagonal wurtzite structure (Fig. 1.1). The crystal can be described as alternating planes composed of tetrahedrally coordinated O^{2-} and Zn^{2+} ions, stacked along the *c*-axis. The physical properties of ZnO semiconductors are presented in Table 1.1.

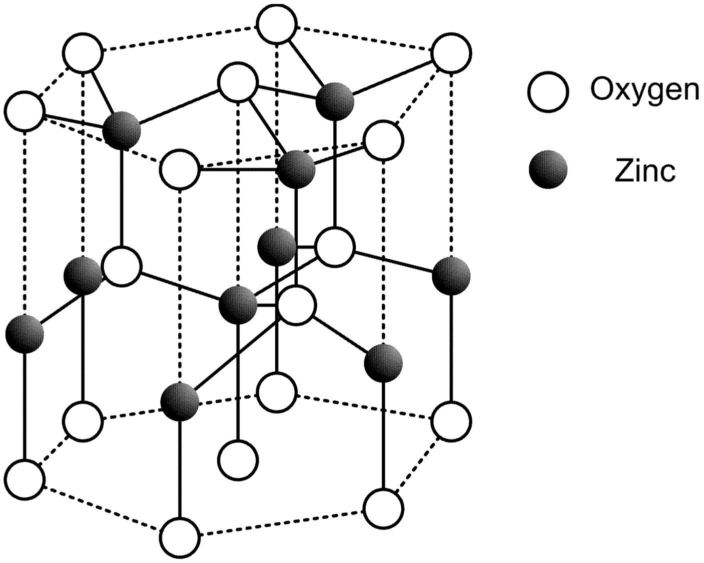

FIG. 1.1. Wurtzite ZnO.

TABLE 1.1. Physical properties of wurtzite ZnO [14]

Properties	**Values**
Lattice constant	
a_0	0.34296nm
b_0	0.52096nm
Density	5.6 g/cm^3
Melting point	2248K
Relative dielectric constant	8.66
Gap energy	3.4 eV, direct
Intrinsic carrier concentration	$<10^6$ cm^{-3}
Exciton binding energy	60 meV
Electron effective mass	0.24
Electron mobility	200 cm^2/V.s
Hole effective mass	0.59
Hole mobility	5-50 cm^2/V.s

1.4 Electrical and optical properties of ZnO

1.4.1 Electrical properties

As grown ZnO usually exhibits n-type conductivity. Intrinsic defects such as zinc interstitials (Zn_i) or oxygen vacancies (V_O) have been claimed to be responsible for n-type conductivity [15,16]. However, the contribution of oxygen vacancies to conductivity has been controversial. Theoretical calculations pointed out that oxygen vacancies are deep donors rather than shallow donors [17,18]. It is also relativity easy to increase n-type conductivity by doping with Al, Ga, or In [19–21]. Furthermore, incorporation of hydrogen can cause n-type conductivity in bulk ZnO [22], and it was theoretically shown that hydrogen acts as a shallow donor [23]. Growth of p-type ZnO is still difficult and reports are controversial [24]. Among the p-type dopants, nitrogen appears to be a promising acceptor for ZnO [25].

The surface properties play an important role in the electrical behavior of ZnO. As presented by Schmidt *et al.* [26–28], the electrical conductivity of high resistivity bulk ZnO is strongly influenced by the sample ambient. The semi-insulating sample can be transformed into a conductive state under vacuum. They explained this behavior in terms of a surface conductive channel that exists in vacuum, but is destroyed upon exposure to air. They proposed that the surface conducting layer is eliminated in air due to changes in the surface bonds.

1.4.2 Optical properties

The high efficiency of luminescence in the UV to visible regions of the spectrum makes ZnO an attractive material for optoelectronic applications. The near-bandgap emission is due to recombinations of free electrons in the conduction band and holes in the valence band. A broadband emission within the visible region, due to transitions involving defect states, is a common photoluminescence feature of bulk ZnO [29]. Impurity atoms also contribute to visible emission; e.g., green luminescence from Cu acceptors in ZnO [30,31].

In the nanoscale, the quantum confinement effect in ZnO nanoparticles was demonstrated by Shim and Guyot-Sionnest [32,33]. The nanoparticles were made n-type by electron transfer doping. The nanoparticles exhibited strong mid-IR absorption due to intraband transitions of electrons in the conduction band (free-carrier absorption). Since nanoparticles have a large surface area, Dijken *et al.* [34] investigated the role of adsorbed oxygen on the emission properties of ZnO nanoparticles. The adsorbed oxygen traps the photogenerated electron and influences the visible emission process.

1.5 Phonons in ZnO

Wurtzite ZnO possesses four atoms per unit cell. Thus, there are 12 phonon branches (3 acoustic branches and 9 optical branches). The optical phonons at the Γ-point belong to following irreducible representation,

$$\Gamma^{\text{opt}} = 1A_1 + 2B_1 + 1E_1 + 2E_2. \tag{1.3}$$

The A_1 and E_1 modes are both Raman and IR active, whereas the E_2 mode is only Raman active. The B_1 modes are inactive to both Raman and IR. In the A_1 and E_1 modes, the atoms oscillate parallel and perpendicular to the c-axis, respectively. The frequencies of optical phonons range from 98 cm^{-1} to 591 cm^{-1} at the Γ-point [35].

1.6 Synthesis of ZnO nanostructures

Zinc oxide nanoparticles have been synthesized by variety of methods. The use of precursor materials such as zinc acetate, zinc nitrate, or zinc carbonate provides an efficient way to synthesize the ZnO nanoparticles. The most common method is the addition of NaOH or LiOH to a zinc acetate solution [36–38]. The overall reaction can be written as:

$$\mathrm{Zn(CH_3COO)_2} + 2\,\mathrm{NaOH} \rightarrow \mathrm{ZnO} + \mathrm{CH_3COONa} + \mathrm{H_2O}. \tag{1.4}$$

In this method, the growth of the particles is governed by temperature, the water content, and solvents. Growth can be terminated by the addition of organic capping materials such as alkanes. Solution methods can also be used to grow nanostructured ZnO such as nanowires. Well-oriented arrays of nanowires were grown on a substrate under a zinc nitrate aqueous solution [39].

Another method developed by Wang *et al.* [40] used a pyrolytic reaction to produce ZnO nanoparticles. In their method, zinc acetate and sodium hydrogen carbonate were reacted at a certain temperature. They showed that the sizes of the particles can be controlled by the reaction temperature. The reaction by-product, sodium acetate, acts as a capping material to prevent further growth of the ZnO nanoparticles. The sodium acetate was washed away with water after the reaction.

However, a major potential problem is the presence of impurities remaining from precursor materials and reaction products. Orlijskii *et al.* [41] reported that Li and Na impurities act as shallow donors in the ZnO nanoparticles. Hydroxyl (OH) molecules on the surface play an important role in the luminescence properties of ZnO quantum dots [42].

1.7 Magnesium: A hydrogen storage material

Hydrogen has potential as an alternative to carbon-based fuels. Using hydrogen requires a reliable medium for storage and transportation. Among the candidate hydrogen storage materials, magnesium compounds have numerous desirable properties. Magnesium is abundant in nature and it is well known that magnesium hydride (MgH_2)

can store hydrogen with a concentration as high as 7.6 % wt [43].

1.7.1 Magnesium hydride

Magnesium hydride can be formed by the reaction of magnesium with hydrogen gas:

$$\mathrm{Mg} + \mathrm{H_2} \Leftrightarrow \mathrm{MgH_2}. \tag{1.5}$$

However, the desorption and absorption processes require moderately high temperatures and long reaction times. The use of magnesium nanostructures may improve these properties.

1.7.2 Hydrogen production

An alternative application of magnesium and magnesium hydride is to produce hydrogen from reaction with water [44]. Both Mg and MgH_2 react with water and produce magnesium hydroxide [$Mg(OH)_2$] plus hydrogen:

$$\mathrm{Mg} + \mathrm{H_2O} \rightarrow \mathrm{Mg(OH)_2} + \mathrm{H_2}, \tag{1.6}$$

$$\mathrm{MgH_2} + 2\,\mathrm{H_2O} \rightarrow \mathrm{Mg(OH)_2} + 2\,\mathrm{H_2}. \tag{1.7}$$

In hydrogen production and storage applications, a major challenging problem is that the formation of passive layers of $Mg(OH)_2$ and MgO interrupts the further reaction of magnesium metal, preventing the penetration of hydrogen.

IR absorption and Raman spectroscopy of $Mg(OH)_2$ have been performed previously. Sharp IR absorption peaks were found at 3700 cm^{-1} and 2721 cm^{-1} for the OH and OD stretch modes, respectively [45]. Oliveira and Hase [46] observed slightly different results, with frequencies at 3698 cm^{-1} and 2725 cm^{-1}. Other works [47,48] also reported on OH vibrational modes in $Mg(OH)_2$.

1.8 Outline of the dissertation

Although this work focuses on two different materials, semiconducting ZnO and metallic Mg, in fact they are related. Introducing Mg atoms into a ZnO host is used to increase the bandgap of ZnO. Zinc oxide nanostructures are also potential candidates for hydrogen storage materials [49,50]. The combination of the two materials may enhance their properties.

Chapter 2 presents a description of the experimental techniques. In Chapter 3, the theoretical background relevant to this work is discussed. Chapter 4 reports the presence of CO_2 molecules in ZnO nanoparticles, observed by IR spectroscopy. Infrared reflectance studies on hydrogenated ZnO nanoparticles are discussed in Chapter 5. The IR optical transition spectra of Cu ions in ZnO nanoparticles are presented in Chapter 6. In Chapter 7, IR spectroscopy of $Mg(OH)_2$ layers on Mg and MgH_2, formed by reaction with water, is presented.

References

[1] *Nanoparticles: From Theory to Application*, edited by G. Schmid, (Wiley-VCH, 2006).

[2] C. F. Bohren, and D. R. Huffman, *Absorption and Scattering of Light by Small Particles*, (Wiley, New York, 1983).

[3] J. S. Blakemore, *Semiconductor Statistics*, (Dover, New York, 1987).

[4] J. D. Bryan and D. R. Gamelin, Prog. Inorg. Chem. **54**, 74 (2005).

[5] W. Hirschwald, P. Bonasewicz, L. Ernst, M. Grade, D. Hofmann, S. Krebs, R. Littbarski, G. Neumann, M. Grunze, D. Kolb, and H. J. Schulz, Curr. Topics Mater. Sci. **7**, 143 (1981).

[6] U. Ozgur, Ya. I. Alivov, C. Liu, A. Teke, M. A. Reshchikov, S. Dogan, V. Avrutin, S. J. Cho, and H. Morkoc, J. Appl. Phys. **98**, 041301 (2005).

[7] Z. L. Wang, J. Phys. D: Appl. Phys. **16**, R829 (2004).

[8] U. Ozgur, and H. Morkoc, in *Zinc Oxide Bulk, Thin Films and Nanostructures: Processing, Properties and Applications*, edited by C. Jagadish, and S, Pearton (Elsevier, Amsterdam, 2006).

[9] J. F. Wager, Science **300**, 1245 (2003).

[10] M. H. Huang, S. Mao, H. Feick,H. Yan, Y. Wu, H. Kind, E. Weber, R. Russo, and P. Yang, Science **292**, 1897 (2001).

[11] N. F. Foster, and G. A. Rozgonyi, Appl. Phys. Lett. **8**, 221 (1966).

[12] W. Fuhs, in *Zinc Oxide-A Material for Micro- and Optoelectronic Applications*, edited by N. H. Nickel and E. Terukov (Springer, Berlin, 2005).

[13] K. Eda, IEEE Electrical Insulation Magazine **5**, 28 (1989).

[14] S. J. Pearton, D.P. Norton, K. Ip, Y.W. Heo, T. Steiner, Progress in Materials Science **50**, 293 (2005).

[15] E. Harrison, Phys. Rev. **93**, 52 (1954).

[16] D. G. Thomas, J. Phys. Chem. Solids **3**, 229 (1957).

[17] C. G. Van de Walle, Physica B **308-310**, 899 (2000).

[18] A. Janotti, and C. G. Van de Walle, Phys. Rev. B **76** 165202 (2007).

[19] S. Y. Myong, S. J. Baik, C. H. Lee, W. Y. Cho, and K. S. Lim, Jpn. J. Appl. Phys., Part 2 **36**, L1078 (1997).

[20] B. M. Ataev, A. M. Bagamadova, A. M. Djabrailov, V. V. Mamedov, and R. A. Rabadanov, Thin Solid Films **260**, 19 (1995).

[21] M. Caglar, Y. Caglar, and S. Ilican, Phys. Status Solidi C **4**, 1337 (2007).

[22] D. G. Thomas, and J. J. Lander, J. Chem. Phys. **25**, 1136 (1956).

[23] C. G. Van de Walle, Phys. Rev. Lett. **85**, 1012 (2000).

[24] D. C. Look, and B. Claflin, Phys. Stat. Sol. (b) **241**, 624 (2004).

[25] A. Tsukazaki et al., Nat. Mater. **4**, 42 (2005).

[26] O. Schmidt, P. Kiesel, C. G. Van de Walle, N. M. Johnson, J. Nause, and G. H. Dohler, Jpn. J. Appl. Phys. **44**, 7271 (2005).

[27] O. Schmidt, A. Geis, P. Kiesel, C. G. Van de Walle, N. M. Johnson, A. Bakin, A. Waag, and G. H. Dohler, Superlattice and Microstructure **39**, 8 (2006).

[28] O. Schmidt, P. Kiesel, D. Ehrentraut, T. Fukuda, and N. M. Johnson, Appl. Phys. A **88**, 71 (2007).

[29] B. K. Meyer, H. Alves, D. M. Hofmann, W. Kriegseis, D. Forster, F. Bertram, J. Christen, A. Hoffmann, M. StraSSburg, M. Dworzak, U. Haboeck, A. V. Rodina, Phys. Stat. Sol. (b) **241**, 231 (2004).

[30] P. Dahan, V. Fleurovy, P. Thurianz, R. Heitzz, A. Hoffmannz, and I. Broserz, J. Phys. Condens. Matter **10**, 2007 (1998).

[31] N. Y. Garces, L. Wang, L. Bai, N. C. Giles, L. E. Halliburton, and G. Cantwell, Appl. Phys. Lett. **81**, 622 (2002).

[32] M. Shim, and P. Guyot-Sionnest, Nature, **407**, 981 (2000).

[33] M. Shim, and P. Guyot-Sionnest, J. Am. Chem. Soc, **123**, 11651 (2000).

[34] A. van Dijken, E. A. Meulenkamp, D. Vanmaekelbergh, and A. Meijerink, J. Phys. Chem. B **104**, 4355 (2000).

[35] P. Y. Emelie, J. D. Phillips, B. Buller, and U. D. Venkateswaran, J. Electron. Mater. **35**, 525 (2006).

[36] L. Spanhel, and M. A. Ansderson, J. Am. Chem. Soc. **113**, 2826 (1991).

[37] E. A. Melenkamp, J. Phys. Chem. B **102**, 5566 (1998).

[38] Z. Hu, G. Oskam, and P. C. Searson, J. Colloid Interface Sci. **263**, 454 (2003).

[39] L. E. Greene, M. Law, J. Goldberger, F. Kim, J. C. Johnson, Y. Zhang, R. J. Saykally, and P. Yang, Angew. Chem. Int. Ed. **42**, 3031 (2003).

[40] Z. Wang, H. Zhang, L. Zhang, J. Yuan, S. Yan and C. Wang, Nanotechnology **14**, 11 (2003).

[41] S. B. Orlinskii, J. Schmidt, P. G. Baranov, D. M. Hofmann, C. M. Donega, and A. Meijerink, Phys. Rev. Lett. **92**, 047603 (2004).

[42] H. Zhou, H. Alves, D. M. Hofmann, B. K. Meyer, G. Kaczmarczyk, A. Hoffmann, and C. Thomsen, Phys. Status Solidi B **229**, 825 (2002).

[43] *Hydrogen Energy System: Production and Utilization of Hydrogen and Future*, edited by Y. Yurum, (Springer, 1995).

[44] M. H. Grosjean, M. Zidounce, and L. Rouce, Journal of Alloys and Compounds, **404-406**, 712 (2005).

[45] R. A. Buchanan, H. H. Caspers, and J. Murphy, Appl. Opt. **2**, 1147 (1963).

[46] E. F. de Oliveira, and Y. Hase, Vibrational Spectroscopy **25**, 53 (2001).

[47] R. T. Mara, and G. B. B. M. Sutherland, J. Opt. Soc. Am. **43**, 1100 (1953).

[48] H. A. Benesi, J. Chem. Phys. **30**, 852 (1959).

[49] Q. Wan, C. L. Lin, X. B. Yu, and T. H. Wang, Appl. Phys. Lett. **84**, 124 (2004).

[50] H. Pan, J. Luo, H. Sun, Y. Feng, C. Poh, and J. Lin, Nanotechnology, **17**, 2963 (2006).

CHAPTER 2

EXPERIMENTAL TECHNIQUES

2.1 Fourier transform infrared (FTIR) spectroscopy

The principal experimental method in this work is Fourier transform infrared [1–4] spectroscopy, which allows us to detect infrared (IR) absorption and reflection properties over a broad spectral region.

An FTIR is based on a Michelson interferometer, which consists of a beam splitter, a fixed mirror and a moving mirror (scanning mirror). As shown in Fig. 2.1, light from the source is separated into two parts and then recombines at the beam splitter after reflection by the two mirrors. Due to the path difference between the two beams, an interference pattern is generated. The output beam from interferometer is recorded as a function of path difference, and is called the interferogram (Fig. 2.2). The IR spectrum can be obtained by calculating the Fourier transform of the interferogram.

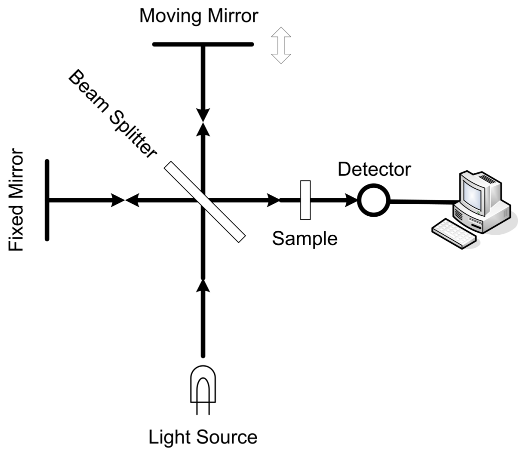

FIG. 2.1. Schematic diagram of an FTIR.

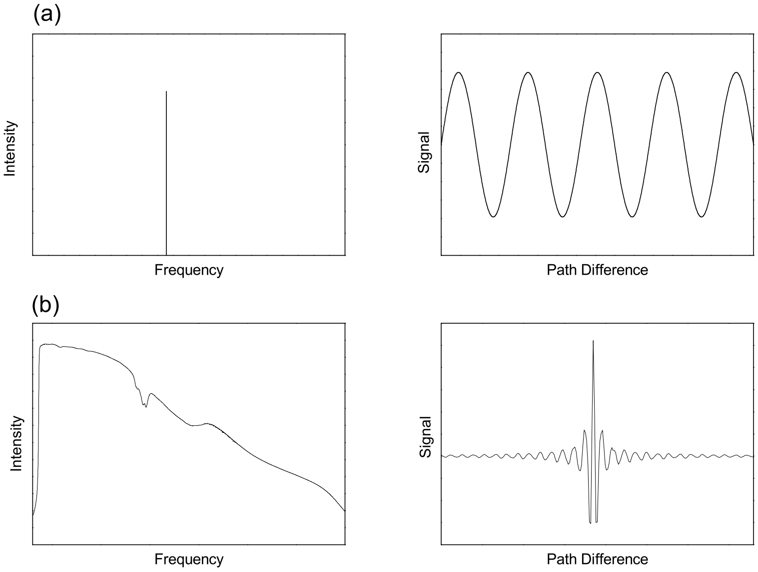

FIG. 2.2. Spectra and interferograms for (a) monochromatic light and (b) broadband light.

2.2 Fourier transform technique

In this section, I will follow the treatment given in Ref. [1]. Mathematically, a Fourier pair $y(x)$ and $E(k)$ can be represented by:

$$y(x) = \int_{-\infty}^{\infty} E(k) \exp(2\pi ikx) dk, \tag{2.1}$$

$$E(k) = \int_{-\infty}^{\infty} y(x) \exp(-2\pi ikx) dx. \tag{2.2}$$

Consider two electromagnetic waves, $y_1(x)$ and $y_2(x)$, seperated by a path difference δ:

$$y_1(x) = \int_{-\infty}^{\infty} E(k) \exp(2\pi ikx) dk, \tag{2.3}$$

$$y_2(x) = \int_{-\infty}^{\infty} E(k) \exp[2\pi ik(x - \delta)] dk. \tag{2.4}$$

The superposition of two waves results in

$$y(x) = y_1(x) + y_2(x) = \int_{-\infty}^{\infty} E(k)[1 + \exp(-2\pi ik\delta)] \exp(2\pi ikx) dk. \tag{2.5}$$

Let us define the resultant field $E(\delta, k)$ as

$$y(x) = \int_{-\infty}^{\infty} E(\delta, k) \exp(2\pi ikx) dk. \tag{2.6}$$

By comparing Eq. 2.5 and Eq. 2.6,

$$E(\delta, k) = E(k)[1 + \exp(-2\pi i k\delta)]. \tag{2.7}$$

The intensity $B(\delta, k)$ is given by

$$B(\delta, k) = \frac{1}{2} c\varepsilon_0 E^*(\delta, k) E(\delta, k), \tag{2.8}$$

where ε_0 is the permittivity of free space and c is the velocity of light. Plugging in for $E(\delta, k)$ yields

$$B(\delta, k) = c\varepsilon_0 E^2(k)\big[1 + \cos(2\pi\delta k)\big]. \tag{2.9}$$

For a broadband source,

$$I(\delta) = c\varepsilon_0 \left[\int_0^\infty E^2(k)dk + \int_0^\infty E^2(k)\cos(2\pi\delta k)dk \right]. \tag{2.10}$$

If the path difference between the two beams is zero ($\delta = 0$), Eq. 2.10 becomes

$$\frac{1}{2} I(0) = c\varepsilon_0 \int_0^\infty E^2(k)dk. \tag{2.11}$$

Substituting Eq. 2.11 into Eq. 2.10 yields

$$\left[I(\delta) - \frac{1}{2} I(0) \right] = \int_0^\infty c\varepsilon_0 E^2(k)\cos(2\pi\delta k)dk. \tag{2.12}$$

Using a Fourier transform, we get

$$c\varepsilon_0 E^2(k) = \int_0^\infty [I(\delta) - I(0)] \cos(2\pi k\delta) d\delta. \tag{2.13}$$

The final result is obtained as

$$B(k) = (\text{constant}) \int_0^\infty \left\{ \left[I(\delta) - \frac{1}{2} I(0) \right] \cos(2\pi k\delta) \right\} d\delta. \tag{2.14}$$

In general form, we can rewrite the above expression as

$$B(k) = \int_{-\infty}^\infty \left[I(\delta) - \frac{1}{2} I(0) \right] \exp(-2\pi i k\delta) d\delta. \tag{2.15}$$

The fast Fourier transform (FFT) method [5] can be used to obtain the spectrum from the interferogram.

2.3 Apodization

The integration limits in the mathematical forms of the Fourier transform in Eqs. 2.14 and 2.15 are extended to infinity. However, this is impractical for an FTIR, since the moving mirror travels only a finite distance. The Fourier transform of a truncated interferogram results in a spectrum where peaks are surrounded by side lobes.

If the interferogram is collected between $\delta - L$ and $\delta + L$, it is equivalent to multiplying the ideal interferogram by a boxcar function $f(x)$ [6]:

$$f(x) = \begin{cases} 1 & \mid x \mid \leq L \\ 0 & \mid x \mid > L. \end{cases} \tag{2.16}$$

The Fourier transform of boxcar function is a sinc function [$\mathrm{sinc}(x) = \sin(x)/x$] (Fig. 2.3). It can be seen that the convolution of the sinc function introduces a series of positive and negative side lobes (Fig. 2.3). The side lobes can be suppressed by multiplying the interferogram with a suitable apodization function such as a Triangular function prior to performing the FFT:

$$f(x) = \begin{cases} 1 - \frac{|x|}{L} & \mid x \mid \leq L \\ 0 & \mid x \mid > L. \end{cases} \tag{2.17}$$

The Fourier transform of a triangular function is $\mathrm{sinc}^2(x) = \sin^2(x)/x^2$. As shown in Fig. 2.3, the side lobes are considerably reduced.

Happ-Genzel [7] and Norton-Beer [8] functions are most commonly used for apodization.

Happ-Genzel:

$$f(x) = a + b \cos\left(\frac{x\pi}{2L}\right). \tag{2.18}$$

Norton-Beer:

$$f(x) = \sum_{n=0}^{k} C_n \left[1 - \left(\frac{x}{L}\right)^2\right]^n; \qquad \sum_{n=0}^{k} C_n = 1. \tag{2.19}$$

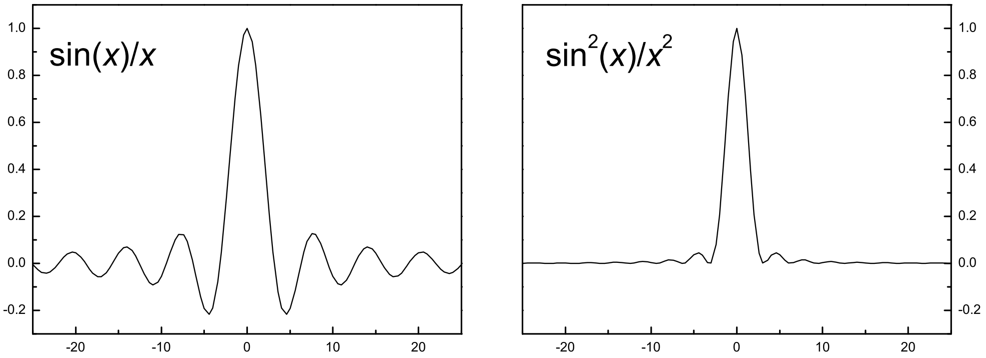

FIG. 2.3. Plots of $\sin(x)/x$ and $\sin^2(x)/x^2$ functions.

2.4 Phase correction

Ideally, the interoferogram should be perfectly symmetrical around zero path differnce (ZPD). However, in practice, the collected interferogram is somewhat asymmetrical. This effect is due to a phase shift in incident light that results from optical components such as the beam splitter, mirrors and recording equipment. The asymmetric interferograms require a phase correction to obtain the correct spectra. If a phase error $\Theta(k)$ is associated in the asymmetic interferogram, the correlation between the true spectrum $B(k)$ and measured spectrum will be

$$B(k)\exp[-i\Theta(k)] = S(k), \tag{2.20}$$

where $S(k)$ denotes the Fourier transform of the asymmetric interferogram. The phase error function $\Theta(k)$ is given by

$$\Theta(k) = \arctan\left\{\frac{\mathrm{Im}[S(k)]}{\mathrm{Re}[S(k)]}\right\}, \tag{2.21}$$

For more details on the phase correction method, the reader is referred to Ref. [9].

2.5 Resolution of an FTIR spectrometer

The resolution of an FTIR spectrometer is given by

$$\Delta \sim \frac{1}{\delta_{max}}, \tag{2.22}$$

where Δ is the resolution in wavenumbers (cm^{-1}) and δ_{max} is maximum path difference, which is twice the distance of mirror travel distance in centimeters.

2.6 Advantages of an FTIR

There are two primary advantages to using an FTIR spectrometer as compared to a dispersive spectrometer, Fellgett's advantage and Jacquinot's advantage.

Fellgett's advantage (Multiplex advantage): Generally, the signal-to-noise ratio (SNR) is proportional to the number of scans or measurement time T (SNR $\propto \sqrt{T}$). In a broadband spectrum, the number of spectral elements n between the frequency range ν_1 and ν_2 can be defined as $n = (\nu_2 - \nu_1)/\Delta\nu$. In a dispersive spectrometer, a particular spectral element is recorded in a time t, so that the total time required is $T = nt$. However, the FTIR spectrometer records information for all wavelengths in the spectrum simultaneously. During each scan, it records n times faster than a dispersive spectrometer with the same SNR. If the measurement time is the same, then the SNR will be increased by factor of $\sqrt{n}$.

Jacquinot's advantage (Throughput advantage): In a dispersive spectrometer the energy throughput is limited by the entrance and exit slits of the monochromator. Since the FTIR does not require slits, measurements at higher intensities are possible. To increase the resolution of a dispersive spectrometer, the slits must be narrowed. In an FTIR, resolution is increased by increasing mirror travel distance (section 2.5) with no decrease in energy throughput.

2.7 Spectrometer components and operating frequency range

The operating frequency range of an FTIR depends on three components: the light source, beam splitter, and detector. The most common type of IR light source is a high temperature ceramic, which is a black body radiator. The beam splitter consists of a thin film deposited on a non-absorbing substrate. Ge coated KBr, and Sn_2Sb_3 coated CaF_2 beam splitters are frequently used for the mid-IR region. Far-IR beam splitters are made of Mylar thin films. Infrared detectors are generally classified into two types, quantum and thermal. In quantum type detectors such as HgCdTe and InSb, free electrons excited by IR photons create the electrical signals. The dectector must be cooled down, typically to liquid nitrogen temperatures, to reduce the thermally excited current. The thermal type, such as the DTGS (Deuterated Tri-Glycine

Sulfate) detector, uses the pyroelectric effect. The temperature changes in pyroelectric material, due to absorption of IR photons, causes changes in the polarization and produces a detectable electric signal. However, the detector response and sensitivity of thermal type detectors are lower than that of quantum type detectors. The typical spectral ranges of the different components are summarized in Table 2.1.

TABLE 2.1. Operating spectral ranges of BOMEM DA8 FTIR components [10].

Components	**Materials**	**Range (cm^{-1})**
Light Source	Globar	200-10000
	Quartz	2000-25000
Beam splitter	Mylar	125-850
	KBr	450-4000
	CaF_2	1200-8500
Detector	DTGS	10-700
	HgCdTe(MCT)	400-5000
	InSb	1800-14000

2.8 BOMEM DA8 FTIR spectrometer

A BOMEM DA8 FTIR spectrometer (Fig. 2.4) was used in this work. It is versatile and is capable of attaining 0.02 cm^{-1} resolution. The upper section of the spectrometer contains the light source and beam splitter compartment. Light from the source passes through an aperture (an adjustable mechanical iris) and optical filter before reaching the beam splitter. The sample compartment and interchangeable detector modules are located in the middle section (Fig. 2.5). An ellipsoidal mirror is used in the detector module to focus the light into the detector. A beam switching mirror is situated in the middle section so that the IR light beam can be directed to the different ports.

The lower section contains vacuum leads, preamplifiers and control electronics. The spectrometer is evacuated by a vacuum pump to minimize the unwanted absorption of CO_2 and H_2O molecules from the air. The vacuum also prevents degradation of the hygroscopic KBr beam splitter. The spectrometer is connected to a computer via an ethernet cable, and the spectrometer control and data acquisition are performed by BOMEM PCDA software.

The accurate position of the moving mirror is measured by detecting the interference pattern of a He-Ne laser (632 nm), sent through coaxially with the IR beam path in the interferometer. The precise distance of the scanning mirror travel is obtained by counting the number of fringes. In addition, a white light source is used to determine the zero path difference (ZPD) position, since white light produces maximum intensity at ZPD. A beam splitter for the visible region is mounted at the center of the IR beam splitter. Dynamic alignment provides accurate alignment of the fixed mirror during each scan.

2.9 Absorption and transmission

2.9.1 Beer-Lambert law

The relationship between the intensities of the incident (I_0) and transmitted (I_T) beam is determined by the Beer-Lambert law,

$$I_T = I_0 \exp(-\alpha d). \tag{2.23}$$

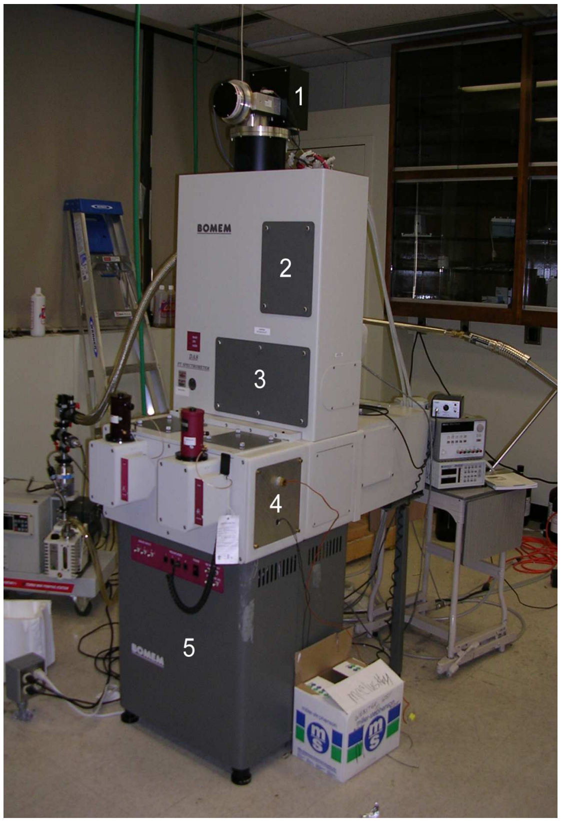

FIG. 2.4. BOMEM DA8 FTIR spectrometer. (1) Scanning motor, (2) Source compartment, (3) Beam splitter compartment, (4) Sample compartment and detector modules, and (5) Electronic compartment.

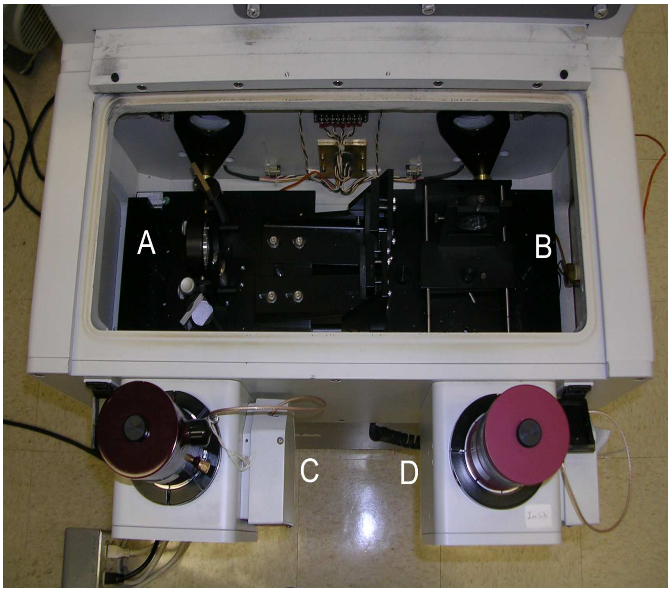

FIG. 2.5. Sample compartment (A) Reflection mode, (B) Transmission mode, and (C, D) detectors.

In logarithmic form,

$$-\log\left(\frac{I_T}{I_0}\right) = \alpha d, \tag{2.24}$$

where α is the absorption coefficient and d is the thickness of the sample.

The transmission T is defined as

$$T = \frac{I_T}{I_0}. \tag{2.25}$$

Thus,

$$\log\left(\frac{1}{T}\right) = \alpha d. \tag{2.26}$$

2.9.2 Integrated absorbance

The integrated absorbance $\overline{A}$ is defined as

$$\overline{A} = \int \alpha(\nu) d\nu. \tag{2.27}$$

The integrated absorbance is useful in cases where the absorption band shape or width changes with increasing (or decreasing) concentration of the sample.

2.10 Infrared reflectance spectroscopy

In our IR reflectance spectroscopy measurements, the spectra are taken with a near-normal incidence configuration (Fig. 2.6). The reflectance set-up is built with two flat mirrors and two concave mirrors. A gold mirror is used as a reference.

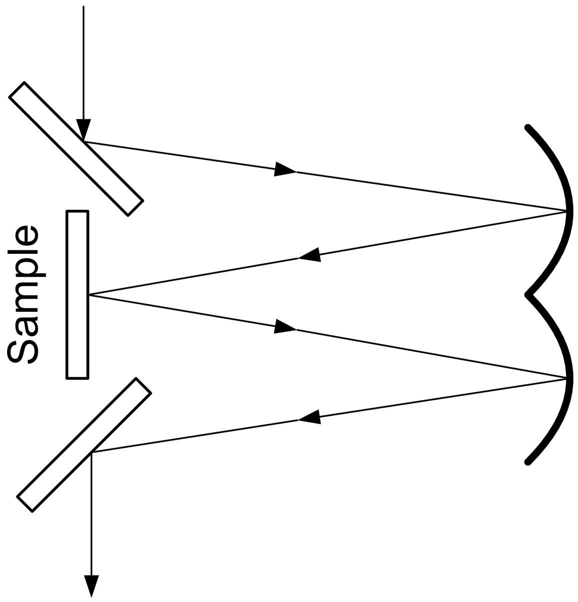

FIG. 2.6. Near-normal reflectance configuration.

The reflectance R is defined as the ratio of reflected intensity I_R to incident intensity I_0:

$$R = \frac{I_R}{I_0}. \tag{2.28}$$

A detailed discussion on the reflectance properties of materials is given in Chapter 3.

2.11 Sample preparation for powder samples

Powder samples were made into solid pellets to measure their IR spectra. A commercial hand press and die sets were used for the sample preparation. A hand press consists of a movable cylinder press controlled by a lever capable of applying pressure to the sample. The powder is loaded into a die set (a 7 mm diameter die set was used in this work), and placed into the hand press to apply the pressure. An adjustable dial is used to set the position of the press, and the exerted force can be controlled for the purpose of reproducibility of the pellets. Some samples are required to be diluted in a non-absorbing medium such as KBr powder to measure the IR transmission spectrum.

2.12 Electrical measurements

2.12.1 Conductivity

The conductivity σ of a material is determined by its free-carrier concentration n and mobility μ of the free carriers:

$$\sigma = ne\mu, \tag{2.29}$$

where e is charge of an electron. The reciprocal of σ is electrical resisitivity $\rho = 1/\sigma$.

2.12.2 Van der Pauw method

The 4-probe method in the Van der Pauw geometry [11,12] is a widely used method to measure the conductivity, carrier concentration and mobility of a sample. In this method, four small ohmic contacts were placed on the periphery of the sample (Fig. 2.7). An advantage of the Van der Pauw method is its usefulness for arbitrarily shaped samples, since the geometric spacing of the contacts is not an issue.

To measure the resistivity, a current i_{MN} was applied into point M and out of point N, and the potential difference between point P and O was measured. The resistance $R_{MN,OP}$ is defined as

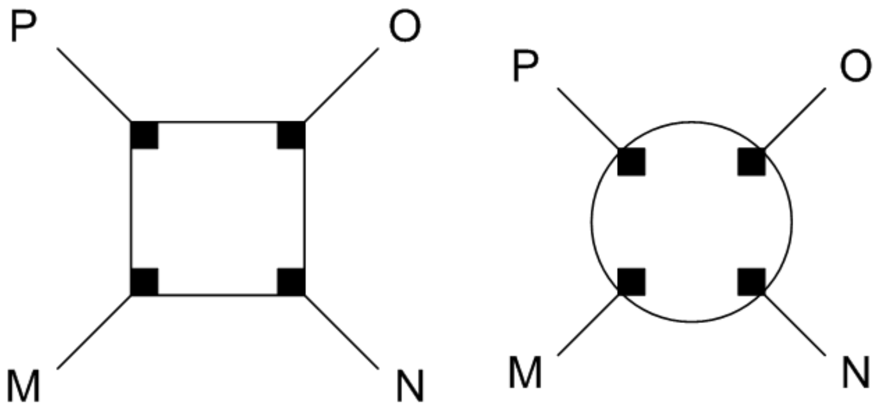

FIG. 2.7. Electrical contacts on the samples with different shapes.

$$R_{MN,OP} = \frac{V_P - V_O}{i_{MN}}. \tag{2.30}$$

Similarly the resistance $R_{NO,PM}$ is

$$R_{NO,PM} = \frac{V_M - V_P}{i_{NO}}. \tag{2.31}$$

More precise results can be achieved by taking several measurements in forward and reverse polarities, and averaging.

Van der Pauw showed that the resisitivity ρ is determined by

$$\exp\left(-\frac{\pi d}{\rho}R_{MN,OP}\right) + \exp\left(-\frac{\pi d}{\rho}R_{NO,PM}\right) = 1, \tag{2.32}$$

where d is the thickness of the sample.

Equation (2.32) can be simplified as

$$\rho = \frac{\pi d}{\ln 2} \frac{R_{MN,OP} + R_{NO,PM}}{2} f. \tag{2.33}$$

The factor f is a function only the ratio $R_{MN,OP}/R_{NO,PM}$. If the sample is symmetric, the resisitivity is given by

$$\rho = \frac{\pi d}{\ln 2} R. \tag{2.34}$$

In this work, we used a MMR Technologies, Inc. variable temperature Hall measurement system, which is capable of operating a temprature range from 80 K to 700 K. The system includes a Hall dewar, K-20 programmable temperature controller, and H-50 interface. The Hall dewar is a vacuum tight chamber. A thermocouple and heating wire are mounted underneath the cold stage. The dewar applies the Joule-Thomson effect to achieve the low temperatures. High pressure nitrogen gas is allowed to expand adiabatically through a capillary tube, and the gas cools down. The desired temperature is maintained by the K-20 controller. The applied current and voltage between probes are controlled by the H-50 interface. The sample is mounted on a cold stage and placed inside the Hall dewar (dark environment) to avoid the photoconductive effect during the measurement.

2.13 Other experimental techniques

This section presents a brief description of complementary experimental techniques used to obtain the results in this dissertation.

2.13.1 Raman spectroscopy

Raman spectroscopy is based on inelastic scattering of light by materials. When a beam of photons interacts with the material, the vast majority of photons are scattered with unchanged energy. This scattering process is known as *Rayleigh scattering.* Only a small portion of photons are scattered with a energy shift. The energy difference between incident and scattered photons is equal to the vibrational energy of atoms inside the crystal and is called a *Raman shift.* The Raman process can be explained with a classical treatment [13].

The polarization P of a material is related to the polarizability α and incident electric field $E = E_0 \cos(\omega_0 t)$,

$$P = \alpha E_0 \cos(\omega_0 t). \tag{2.35}$$

The normal mode vibration of the atoms with a frequency ω_v is

$$u = u_0 \cos(\omega_v t). \tag{2.36}$$

We can expand α in a Taylor series with respect to normal mode coordinate,

$$\alpha = \alpha_0 + \left(\frac{\partial \alpha}{\partial u}\right) u + \cdots \tag{2.37}$$

Combining Eqs. 2.35-2.37,

$$P = \alpha_0 E_0 \cos(\omega_0 t) + \left(\frac{\partial \alpha}{\partial u}\right) u_0 E_0 \cos(\omega_v t)\cos(\omega_0 t) + \cdots \tag{2.38}$$

The first term of Eq. 2.38 represents Rayleigh scattering, and the second term describes Raman scattering. Using a trigonometric identity we can rewrite the second term as,

$$\left(\frac{\partial \alpha}{\partial u}\right) u_0 E_0 \cos(\omega_v t)\cos(\omega_0 t) = \frac{1}{2}\left(\frac{\partial \alpha}{\partial u}\right) u_0 E_0 \{\cos[(\omega_0 - \omega_v)t] + \cos[(\omega_0 + \omega_v)t]\}. \tag{2.39}$$

The Raman scattered photons are therefore detected at two frequencies, $(\omega_0 - \omega_v)$ and $(\omega_0 + \omega_v)$. The frequencies are known as the Stokes and anti-Stokes frequencies, respectively. Since the Raman process is a weak effect, an intense light source is required in the measurement system to achieve a reliable intensity of scattered photons.

A typical Raman system consists of 3 main components: (a) laser excitation source, (b) monochromator, and (c) detector. The laser beam is focused onto the sample and scattered photons are detected with the monochromator and detector.

Raman spectra were taken with a cw-Kimmon laser (He-Cd laser with a 325 nm wavelength) and JY-Horiba micro-Raman/PL system located at Department of Physics, University of Idaho (Prof. Leah Bergman).

2.13.2 Transmission electron microscopy (TEM)

In a conventional light microscope, the image resolution is limited by the Rayleigh criterion [14],

$$\delta = \frac{0.61\lambda}{\mu \sin \beta}, \tag{2.40}$$

where μ is refractive index of the viewing medium, and β is semi-angle of collection of the magnifying lens. However, a TEM uses electrons instead of photons, and the wavelength λ of electrons is much shorter than that of visible light. Therefore a high resolution image can be obtained. Electrons produced by an electron gun are accelerated by a high voltage electrode and then focused into a small beam by using electromagnetic condenser lenses. A phosphor screen is placed behind the sample, and transmitted electrons are projected onto the screen as an image. The images can be taken in either bright-field mode or dark-field mode. In a bright-field image, only the direct transmitted beam is collected, while the scattered electrons are collected in a dark-field image.

For sample preparation, the nanoparticles were suspended in ethanol and the solvent was dropped onto a copper grid. The TEM images were taken by Prof. Grant Norton's group at WSU. A Philips CM200 Transmission Electron Microscope was used.

2.13.3 X-ray diffraction (XRD)

Each crystalline solid has a unique XRD pattern to identify its crystal structure. When X-ray light with a wavelength λ is incident on a crystal, a diffraction peak occurs if the Bragg condition is satisfied:

$$n\lambda = 2d \sin\theta, \tag{2.41}$$

where d is the lattice spacing of the crystal and θ is the angle of incidence. The Cu K_α emission ($\lambda = 1.5418$ Å) from a copper target is the most common X-ray source for the diffraction measurement. Furthermore, a powder XRD pattern is also used to determine the average size of the nanoparticles. The particle size L can be calculated by using the Scherrer formula:

$$L = \frac{0.9\lambda}{\Delta \cos\theta}, \tag{2.42}$$

where λ is the wavelength of the X-ray, and Δ is width (in radians) of the peak at 2θ.

The XRD measurements were performed at the GeoAnalytical Laboratory, WSU, with a Siemens D-500 X-ray powder diffractometer. The powder sample was smeared onto a quartz slide with an organic solvent such as ethanol or acetone to measure the diffraction pattern.

References

[1] R. J. Bell, *Introductory Fourier Transform Spectroscopy* (Academic Press, New York, 1972).

[2] P. R. Griffiths and J. A. de Haseth, *Fourier Transform Infrared Spectrometry* (Wiley, New York, 1986).

[3] J. B. Bates, Science **191**, 31 (1976).

[4] W. D. Perkins, J. Chem. Educ. **63**, A5 (1986).

[5] J. W. Cooley and J. W. Turkey, Math. Computat. **19**, 297 (1965).

[6] J. F. Rabolt and R. Bellar, Appl. Spectroscopy **35**, 132 (1981).

[7] H. Happ and L. Genzel, Infrared Phys. **1**, 39 (1961).

[8] R. H. Norton and R. Beer, J. Opt. Soc. Am. **66**, 259 (1976).

[9] M. L. Forman, W. H. Steel and G. A. Vanasse, J. Opt. Soc. Am. **56**, 59 (1966).

[10] *The DA8 Series FT-IR Spectrometer Catalog* (Bomem Inc., Quebec).

[11] L. J. van der Pauw, Philips Res. Rept. **13**, 1 (1958).

[12] L. J. van der Pauw, Philips Tech. Rev. **20**, 220 (1958).

[13] A. Schulte, and Y. Guo, in *Handbook of Applied Solid State Spectroscopy*, edited by D. R. Vij (Springer, New York, 2006).

[14] P. E. J. Flewitt, and R. K. Wild, *Physical Methods for Materials Characterisation* (Institute of Physics Publishing, 1994).

CHAPTER 3

THEORY

The purpose of this chapter is to present the theory and relevant equations for the work in Chapter 5.

3.1 Reflectivity and Fresnel's equation

Fresnel's equations describe the propagation of an electromagnetic (EM) wave at an interface (see for example, Ref. [1]). Consider a plane interface between two media, with different refractive indices n_1 and n_2. By applying continuity equations for E and B at the interface, one can relate the incident EM wave to the reflected and transmitted components as follows.

For **E** perpendicular to the plane of incidence,

$$E_i + E_r = E_t, \tag{3.1}$$

$$-\frac{B_i}{\mu_i}\cos\theta_i + \frac{B_r}{\mu_r}\cos\theta_r = -\frac{B_t}{\mu_t}\cos\theta_t, \tag{3.2}$$

for **E** parallel to the plane of incidence,

$$\frac{B_i}{\mu_i} + \frac{B_r}{\mu_r} = \frac{B_t}{\mu_t}, \tag{3.3}$$

$$E_i \cos\theta_i - E_r \cos\theta_r = E_t \cos\theta_t. \tag{3.4}$$

The subscripts i, r and t denote incidence, reflected and transmitted, respectively.

Relating the magnetic fields to the electric fields, and using the above equations, the reflection coefficients are given by Fresnel's equations:

$$\begin{aligned} r_\perp &= \left(\frac{E_r}{E_i}\right)_\perp = \frac{n_1\cos\theta_i - n_2\cos\theta_i}{n_1\cos\theta_i + n_2\cos\theta_t}, \\ r_\parallel &= \left(\frac{E_r}{E_i}\right)_\parallel = \frac{n_2\cos\theta_i - n_1\cos\theta_t}{n_1\cos\theta_t + n_2\cos\theta_i}. \end{aligned} \tag{3.5}$$

The simplest form of Eq. 3.5 occurs at normal incidence, $\theta_i = \theta_r = \theta_t = 0$, in which case the reflectance R is

$$R = |r|^2 = \left|\frac{n_2 - n_1}{n_2 + n_1}\right|^2. \tag{3.6}$$

If we consider the interface between vacuum ($n_1 = 1$) and a medium with $n_2 = \sqrt{\epsilon}$, we can rewrite Eq. 3.6 as

$$R = \left|\frac{\sqrt{\varepsilon} - 1}{\sqrt{\varepsilon} + 1}\right|^2, \tag{3.7}$$

or

$$R = \frac{(n-1)^2 + \kappa^2}{(n+1)^2 + \kappa^2}, \tag{3.8}$$

where ε, n and κ are dielectric function, real and imaginary parts of the refractive index, respectively. The dielectric function is a complex number and frequency dependent.

3.2 Dielectric function

The dielectric function $\varepsilon(\omega)$ describes the linear response of a material to an applied electric field. Valence electrons, phonons and free carriers contribute to the dielectric properties of a material. The valence electrons' contribution to the dielectric function is essentially constant (ε_∞), and is known as the high frequency dielectric constant. Response to light in the IR region is dominated by contributions from phonons and free carriers.

In a presence of an applied electric field $\mathbf{E}$, atoms in the material become polarized. The induced polarization $\mathbf{P}$ is proportional to the applied electric field $\mathbf{E}$ [2]:

$$\mathbf{P} = \epsilon_0 \chi \mathbf{E}, \tag{3.9}$$

where χ is the electric susceptibility of the medium. However, from the definition of the electric displacement $\mathbf{D}$,

$$\mathbf{D} = \epsilon_0 \mathbf{E} + \mathbf{P} = \epsilon_0 (1 + \chi) \mathbf{E} = \epsilon_0 \varepsilon \mathbf{E}. \tag{3.10}$$

We can therefore define the dielectric constant ε as

$$\varepsilon = 1 + \chi. \tag{3.11}$$

3.2.1 Lattice vibration contribution

In a crystal, the atoms are bound to their equilibrium positions. When the atoms move from equilibrium, they oscillate at characteristic frequencies, due to a restoring force. These vibrations are so called phonon [3] modes of the crystal, and have resonant frequencies in the infrared region. There are two types of phonons, longitudinal and transverse. For longitudinal phonons, the displacements of the atoms coincide with the direction of propagation of the wave. For transverse phonons, atoms move perpendicular to the wave propagation. If the crystal has more than one atom in the unit cell, the vibrations of the atoms develop two modes, namely acoustic and optical phonon modes. In a optical phonon mode, any two neighboring atoms oscillate around their equilibrium positions, out of phase with respect to each other. Transverse electromagnetic waves can only couple to transverse optical (TO) modes. However, longitudinal optical phonons (LO) also play an important role in the infrared properties of materials.

Starting from the damped harmonic oscillator equation with resonance frequency ω_{TO} [4]:

$$\mu \frac{d^2x}{dt^2} + \mu\Gamma\frac{dx}{dt} + \mu\omega_{\mathrm{TO}}^2 x = eE_0 \exp(-i\omega t), \tag{3.12}$$

where μ and Γ are the reduced mass and damping factor of the TO phonon, respectively. The solution of Eq. 3.12 is $x = x(0)\exp(i\omega t)$, with

$$x(0) = \frac{eE_0}{\mu(\omega_{\mathrm{TO}}^2 - \omega^2 - i\Gamma\omega)}. \tag{3.13}$$

For a material with N ion pairs with of effective charge e, the polarization P is given by

$$P = \frac{Ne^2E_0}{\mu(\omega_{\mathrm{TO}}^2 - \omega^2 - i\Gamma\omega)}. \tag{3.14}$$

We can combine Eqs. 3.9 and 3.14 to obtain

$$\varepsilon(\omega) = 1 + \chi + \frac{Ne^2}{\mu\epsilon_0}\frac{1}{(\omega_{\mathrm{TO}}^2 - \omega^2 - i\Gamma\omega)}. \tag{3.15}$$

The term χ in Eq. 3.15 represents a non-resonant background. In the limits of low and high frequency, we obtain from above equation

$$\varepsilon(0) = \varepsilon_0 = 1 + \chi + \frac{Ne^2}{\mu\epsilon_0}\frac{1}{\omega_{\mathrm{TO}}^2}, \tag{3.16}$$

and

$$\varepsilon(\infty) = \varepsilon_\infty = 1 + \chi. \tag{3.17}$$

Substituting Eqs. 3.16 and 3.17 into Eq. 3.15, we get

$$\varepsilon(\omega) = \varepsilon_\infty + (\varepsilon_0 - \varepsilon_\infty)\frac{\omega_{\mathrm{TO}}^2}{(\omega_{\mathrm{TO}}^2 - \omega^2 - i\Gamma\omega)}. \tag{3.18}$$

However, the ratio of ε_0 to ε_∞ is given by the Lyddane-Sachs-Teller (LST) relation [5]

$$\frac{\omega_{\mathrm{LO}}^2}{\omega_{\mathrm{TO}}^2} = \frac{\varepsilon_0}{\varepsilon_\infty}. \tag{3.19}$$

Thus, Eq. 3.18 becomes

$$\varepsilon(\omega) = \varepsilon_\infty \left[1 + \frac{\omega_{\mathrm{LO}}^2 - \omega_{\mathrm{TO}}^2}{\omega_{\mathrm{TO}}^2 - \omega^2 - i\Gamma\omega} \right]. \tag{3.20}$$

For a small damping factor $\Gamma = 0$, we can rewrite the above expression as

$$\varepsilon(\omega) = \varepsilon_\infty \left[1 + \frac{\omega_{\mathrm{LO}}^2 - \omega_{\mathrm{TO}}^2}{\omega_{\mathrm{TO}}^2 - \omega^2} \right]. \tag{3.21}$$

From Eq. 3.21, it can be seen that between the ω_{LO} and ω_{TO} frequencies, $\varepsilon(\omega)$ is negative; thus, the refractive index is imaginary. The reflectivity is therefore 1 between the ω_{LO} and ω_{TO}. The strong reflection of infrared radiation between the optical phonon frequencies is known as *reststrahlen* (residual rays) band reflection. A plot of Eq. 3.20 is shown in Fig. 3.1. In non-polar crystals such as Si or Ge, *reststrahlen* band reflection is absent, since $\omega_{\mathrm{LO}} = \omega_{\mathrm{TO}}$.

3.2.2 Free carrier contribution

The doping of a semiconductor leads to an increase in free-carrier concentration. The response of a free carrier to an applied electric field can be described by a classical Drude model. Free electrons are different from bound electrons since the restoration

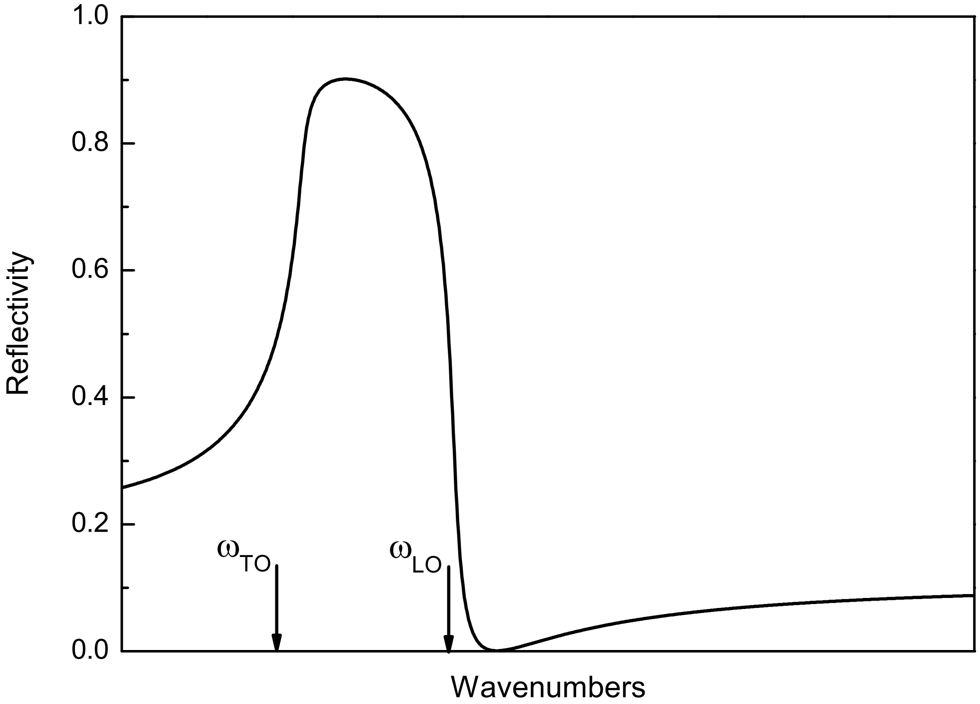

FIG. 3.1. Reststrahlen band reflection.

force on the free electron is zero. The motion of a free electron in external electric field $E_0 \exp(-i\omega t)$ can be modeled by a single harmonic oscillator with a resonance frequency $\omega_0 = 0$:

$$m\frac{d^2x}{dt^2} + m\gamma\frac{dx}{dt} = eE_0 \exp(-i\omega t), \tag{3.22}$$

where m and γ are the mass and damping factor of the electron, respectively. The solution of the above differential equation leads to

$$x(t) = -\frac{e}{m}\frac{1}{(\omega^2 + i\gamma\omega)}E_0 \exp(-i\omega t). \tag{3.23}$$

Since each electron contributes a dipole moment $ex(t)$, the polarization of a medium with a free-electron density n is

$$P = nex(t) = -\frac{Ne^2}{m}\frac{1}{(\omega^2 + i\gamma\omega)}E_0 \exp(-i\omega t). \tag{3.24}$$

Using a similar derivation as in section 3.2.1, the dielectric function $\varepsilon(\omega)$ can be derived as

$$\varepsilon(\omega) = 1 - \frac{\omega_p^2}{(\omega^2 + i\gamma\omega)}, \tag{3.25}$$

where ω_p is the so-called plasma frequency,

$$\omega_p = \sqrt{\frac{ne^2}{\varepsilon_0 m}}. \tag{3.26}$$

For a small damping factor $\gamma = 0$, we can simplify the above expression as

$$\varepsilon(\omega) = 1 - \frac{\omega_p^2}{\omega^2}. \tag{3.27}$$

For frequencies below the plasma frequency, the dielectric constant is negative and the refractive index is purely imaginary. In this region, reflectivity is nearly one, and no electromagnetic wave can propagate into the medium, as evident in most metallic mirrors. This reflection is called plasma reflection. Above the plasma frequency, where the refractive index is real, the electromagnetic waves propagate into the medium and the dielectric function approaches unity at high frequency. Plasma reflection can be seen in both metals and doped semiconductors. A plot of Eq. 3.25 is shown in Fig. 3.2.

3.2.3 Lorentz-Drude model

By combination of Eqs. 3.20 and 3.25, the dielectric function can be written as

$$\varepsilon(\omega) = \varepsilon_\infty \left[1 + \frac{\omega_{\mathrm{LO}}^2 - \omega_{\mathrm{TO}}^2}{\omega_{\mathrm{TO}}^2 - \omega^2 - i\Gamma\omega} - \frac{\omega_p^2}{\omega^2 + i\gamma\omega} \right], \tag{3.28}$$

and is called the Lorentz-Drude model. For a semiconductor with a small free-carrier concentration, the plasma frequency ω_p lies far below the phonon frequencies; hence, contribution from lattice vibrations dominates the dielectric function. When the carrier concentration is large enough to move the plasma frequency into or above the reststrahlen region, there will be changes in the reststrahlen line shape. Calculated reflectance spectra for bulk ZnO samples with different free-carrier concentrations are

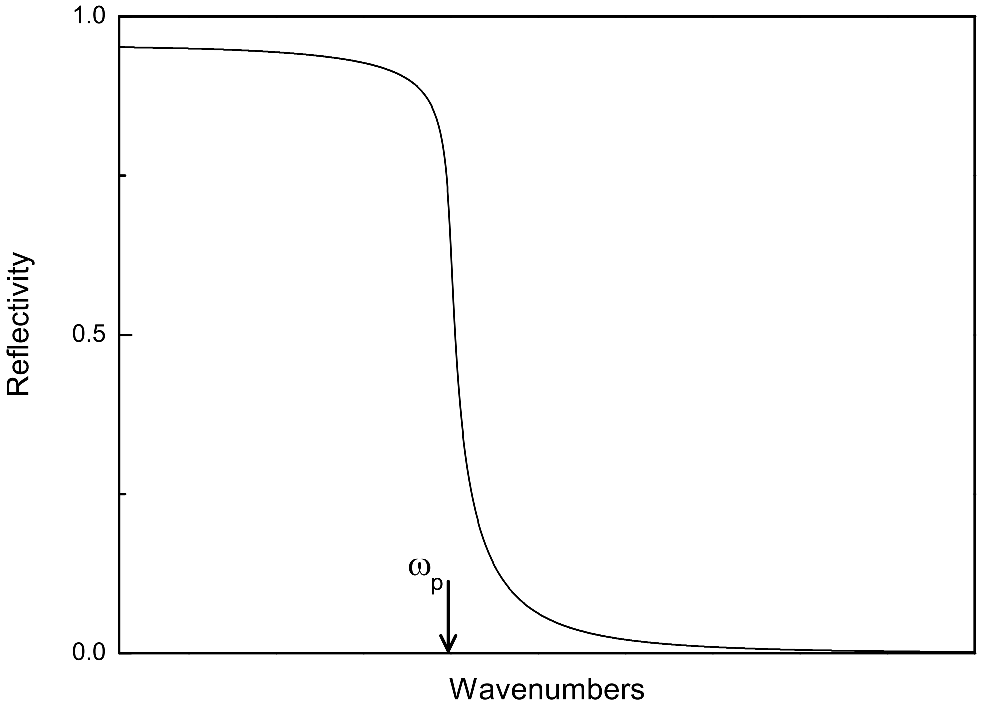

FIG. 3.2. Plasma reflection.

presented in Fig. 3.3. It can be seen that, the high free-carrier concentration in heavily doped sample dominates the reflectivity, with only a weak *reststrahlen* band reflection.

3.3 Surface roughness scattering

The theory described in section 3.1 is based on an ideally smooth surface. However, in practice, we need to consider effect of surface roughness. Due to surface roughness, the reflectance beam can be divided into a specular component and scattering component ($R_{tot} = R_{spec} + R_{diffuse}$). The relationship between the total reflectance and

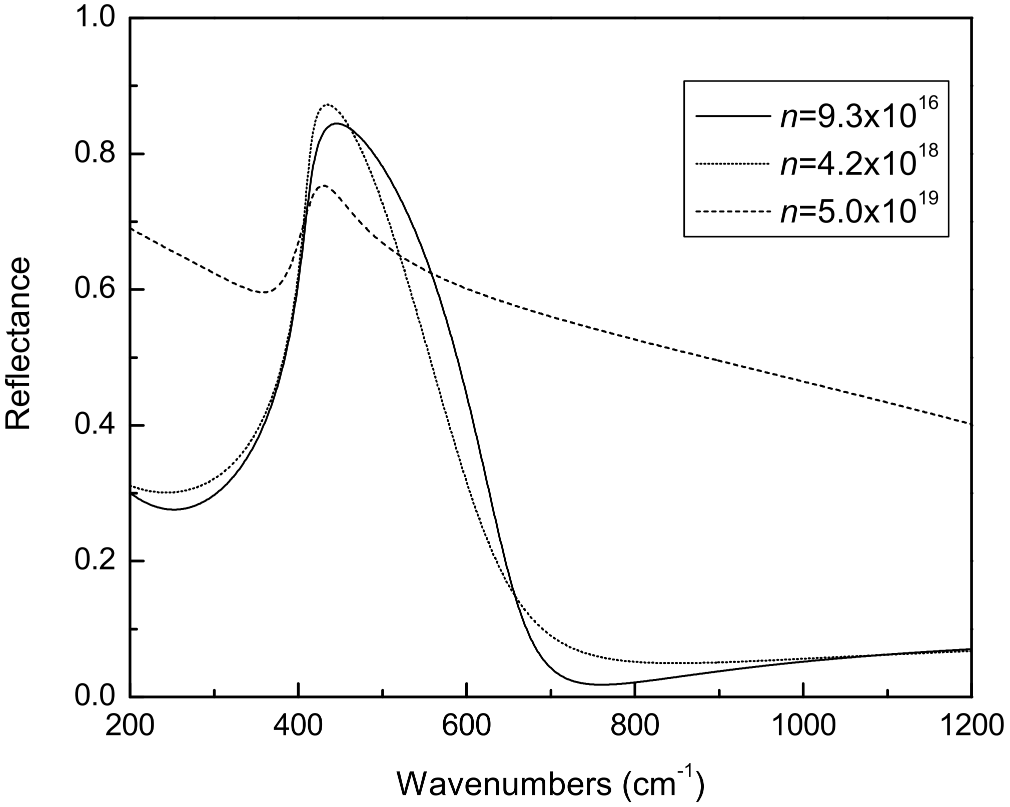

FIG. 3.3. Calculated reflectance spectra of bulk ZnO samples with different free-carrier concentrations. (Data from Ref. [6]).

specular reflectance component is given by [7]

$$\frac{R_{spec}}{R_{tot}} = \exp\left(-\frac{4\pi\delta\cos\theta}{\lambda}\right)^2, \tag{3.29}$$

where δ is the rms value of the surface roughness.

3.4 Absorption and extinction coefficient

A plane electromagnetic wave, propagating along the x-direction, can be described as

$$E(x,t) = E_0 \exp[i(kx - \omega t)]. \tag{3.30}$$

The wave vector in the medium is given by

$$k = \frac{(n + i\kappa)\omega}{c}, \tag{3.31}$$

so that the wave in the medium is

$$E(x,t) = E_0 \exp\left[i\omega\left(\frac{n + i\kappa}{c}x - t\right)\right], \tag{3.32}$$

$$E(x,t) = E_0 \exp\left[i\omega\left(\frac{n}{c}x - t\right)\right] \exp\left(-\frac{\kappa\omega}{c}x\right). \tag{3.33}$$

The above equation is a sinusoidal wave with a damping factor. The intensity is the square of the electric field. Thus, the equation becomes a form of the Beer-Lambert law, with an absorption coefficient $\left(\frac{2\kappa\omega}{c}\right)$:

$$I(x) = I_0 \exp\left(-\frac{2\kappa\omega}{c}x\right). \tag{3.34}$$

Relating $\frac{\omega}{c} = \frac{2\pi}{\lambda}$, we can transform the absorption coefficient $\alpha = \frac{2\omega\kappa}{c}$ to

$$\alpha = \frac{4\pi\kappa}{\lambda}. \tag{3.35}$$

The absorption coefficient α is related to imaginary part of refractive index, which is also called the *extinction coefficeint.*

3.5 Effective medium approximation (EMA)

When the wavelength of the incident electromagnetic wave is much greater than the particle sizes of the inhomogeneous composite material, the material can be treated as a homogeneous material or an effective medium [8]. EMA is a method developed to predict the optical and dielectric properties of a composite as a function of each constituent material, and their volume fractions.

The Clausius-Mossotti relation gives a connection between the macroscopic dielectric function ε and microscopic polarizibility α:

$$\frac{\varepsilon - 1}{\varepsilon + 2} = \frac{1}{3\varepsilon_0} \sum_j n_j \alpha_j, \tag{3.36}$$

where n_j is concentration (per unit volume) of the j^{th} component, and the polarizibility of a spherical particle with dielectric function ε_j, and radius r is given by

$$\alpha = 4\pi\varepsilon_0 r^3 \left(\frac{\varepsilon_j - 1}{\varepsilon_j + 2} \right). \tag{3.37}$$

Combining Eqs. 3.36 and 3.37, we can write

$$\frac{\varepsilon_{\text{eff}} - 1}{\varepsilon_{\text{eff}} + 2} = \sum_j f_j \frac{\varepsilon_j - 1}{\varepsilon_j + 2}. \tag{3.38}$$

The parameter f_j is the volume fraction of the j^{th} component, and $\sum_j f_j = 1$. The above equation is called the Lorentz-Lorenz effective medium expression.

If we consider a host dielectric function ε_h, instead of vacuum, then Eq. 3.38 can be rewritten in the general form:

$$\frac{\varepsilon_{\text{eff}} - \varepsilon_h}{\varepsilon_{\text{eff}} + 2\varepsilon_h} = \sum_j f_j \frac{\varepsilon_j - \varepsilon_h}{\varepsilon_j + 2\varepsilon_h}. \tag{3.39}$$

Based on the above equation, different models have been developed by choosing different host materials. For a composite material, a mixture of materials A and B, the Maxwell-Garnett model [9] assumes that one material acts as the host. Choosing A as the host material ($\epsilon_h = \epsilon_A$), Eq. 3.39 is simplified to

$$\frac{\varepsilon_{\text{eff}} - \epsilon_A}{\varepsilon_{\text{eff}} + 2\varepsilon_A} = f_B \frac{\varepsilon_B - \varepsilon_A}{\varepsilon_B + 2\varepsilon_A}. \tag{3.40}$$

The Maxwell-Garnett model has been successfully applied to explain the optical response of metal-doped stained glasses [11]. However, the model is expected to be satisfactory only in the case of low concentration, in which case the host material and inclusions are not interchangeable.

In some cases, if the volume fractions f_j are comparable to each other, it is unclear how to choose the host material. To solve this quandary, Bruggeman [10] proposed that neither component should play the host role. All materials are considered to be embedded in the effective medium itself, which is equivalent to $\varepsilon_{\text{eff}} = \varepsilon_h$:

$$\sum_j f_j \frac{\varepsilon_j - \varepsilon_{\mathrm{eff}}}{\varepsilon_j + 2\varepsilon_{\mathrm{eff}}} = 0. \tag{3.41}$$

The Maxwell-Garnett (MG) model and Bruggeman (BR) model are the most commonly used models. The difference between the two models is that MG describes inclusions B completely surrounded by the host A, whereas the BR model refers to an aggregate or random mixture where all components are inserted into the effective medium itself (Fig. 3.4).

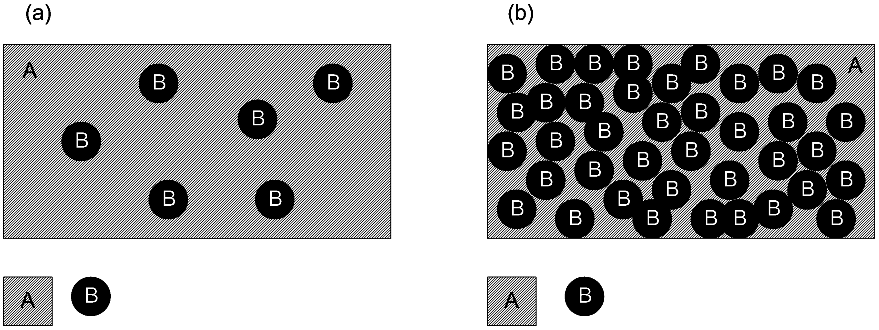

FIG. 3.4. Effective medium models. (a) Maxwell-Garnett, (b) Bruggeman.

References

[1] E. Hecht, *Optics*, 4th Ed. (Addison Wesley, San Francisco, 2002).

[2] J. D. Jackson, *Classical Electrodynamics*, 3rd Ed. (Wiley, New York, 1999).

[3] C. Kittel, *Introduction to Solid State Physics*, 7th Ed. (Wiley, New York, 1996).

[4] P. Y. Yu, and M. Cardona, *Fundamentals of Semiconductors*, (Springer-Verlag, Berlin, 1996)

[5] R. H. Lyddane, R. Sachs, and E. Teller, Phys. Rev. **59**, 673 (1941).

[6] E. F. Venger, A. V. Melnichuk, L. Y. Melnichuk and Y. A. Pasechnik, Phys. Stat. Sol. (b) **188**, 823 (1995).

[7] T. V. Vorburger, E. Marx and T. R. Lettieri, Appl. Optics **32**, 3401 (1993).

[8] D. E. Aspnes, Thin Solid Films, **89**, 249 (1982).

[9] J. C. M. Garnett, Phils. Trans. R. Soc. London **203**, 385 (1904).

[10] D. A. G. Bruggeman, Ann. Phys. (Leipzig) **24**, 636 (1935).

[11] T. Unga, L. M. Liz-Marzanb and P. Mulvaney, Colloids and Surfaces A **202**, 119 (2002).

CHAPTER 4

CARBON DIOXIDE IMPURITIES IN ZINC OXIDE NANOPARTICLES

In this chapter, we report the presence of CO_2 molecules in ZnO nanoparticles, observed by infrared (IR) spectroscopy. Our results revealed that the CO_2 impurities are formed by reactions involving the organic precursors.

4.1 Synthesis of ZnO nanoparticles

The synthesis method described in Ref. [1] was used in this work. Zinc acetate dihydrate [$Zn(CH_3COO)_2 \cdot 2\,H_2O$] and sodium hydrogen carbonate ($NaHCO_3$) were mixed thoroughly at room temperature, with a molar ratio of 1:2.4. The mixture was sealed in an evacuated quartz ampoule filled with 2/3 atm argon gas. In this way, we could prevent contamination from ambient air during the reaction. The reaction was performed at 200 °C for 3 hours. After the reaction process, the product was washed several times with distilled water to remove the by-product sodium acetate (CH_3COONa), and dried at room temperature overnight. The powder was pressed

---

Portions of this chapter were published as: W. M. Hlaing Oo, M. D. McCluskey, A. D. Lalonde, and M. G. Norton, "Infrared spectroscopy of ZnO nanoparticles containing CO_2 impurities." *Appl. Phys. Lett.* **86**, 073111 (2005).

into a thin pellet (thickness 0.25 mm) and then annealed in argon at 350 °C for 2 hours to remove the remaining water.

A transmission electron microscope (TEM) image of the ZnO particles is shown in Fig. 4.1. The particles were roughly spherical, with a size of about 20 nm. The crystal structure was examined by powder X-ray diffraction (XRD) analysis. Three dominant peaks in the (XRD) spectrum (Fig. 4.1) confirmed the hexagonal wurtzite structure, in agreement with previous work [1].

4.2 Vibrations of CO_2 molecules

Room temperature IR absorption spectra were obtained with a Bomem DA8 vacuum Fourier transform infrared (FTIR) spectrometer with a liquid nitrogen cooled HgCdTe detector. The instrumental resolution was 4 cm^{-1}, and the spectra were averaged over 500 scans. As shown in Fig. 4.3 (spectrum a), a strong IR absorption peak was observed at a frequency of 2342 cm^{-1}. In addition, a weak absorption peak was observed at 2277 cm^{-1}. These peaks are assigned to asymmetric stretch frequencies (ν_3) of $^{12}CO_2$ and $^{13}CO_2$ molecules, respectively. For a linear free CO_2 molecule, the ν_3 vibrational frequency is estimated by (APPENDIX A)

$$\nu = \sqrt{\kappa\left(\frac{2}{M_C} + \frac{1}{M_O}\right)}, \tag{4.1}$$

where M_C and M_O are the masses of carbon and oxygen respectively, and κ is an effective spring constant. The calculated frequency ratio of $\nu(^{12}CO_2)$ to $\nu(^{13}CO_2)$

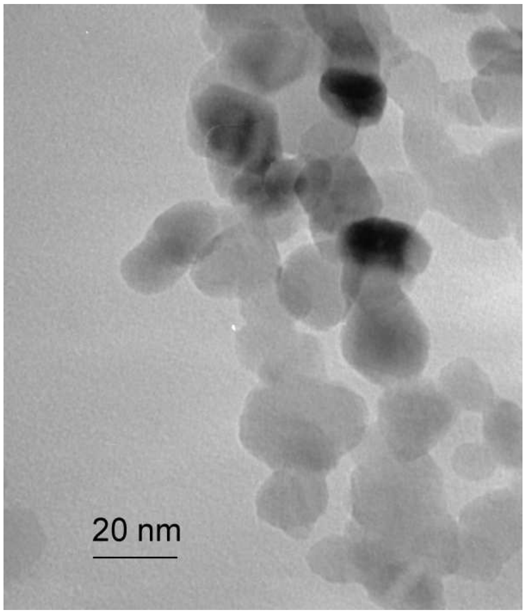

FIG. 4.1. TEM image of ZnO nanoparticles.

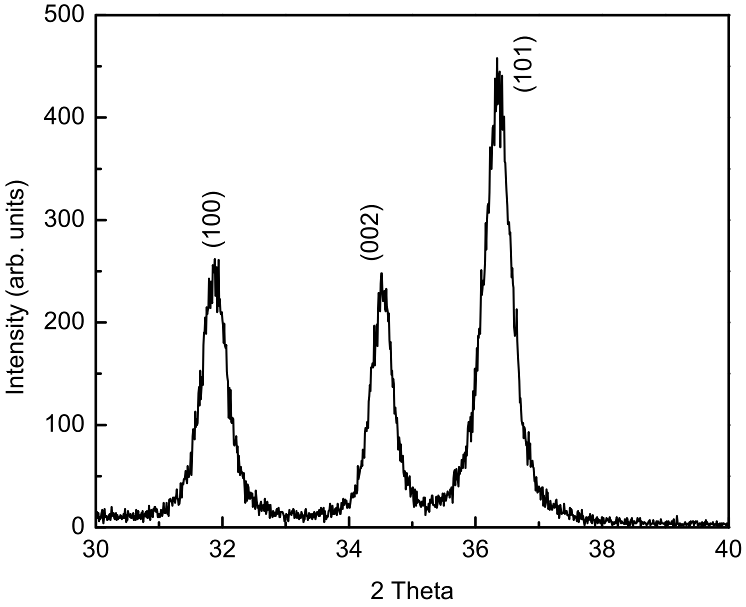

FIG. 4.2. XRD spectrum of ZnO nanoparticles.

is 1.029, in good agreement with the observed ratio of 1.028. The ratio of peak intensities is in agreement with the natural isotopic abundance ([^{13}C]/[^{12}C]=0.01). Broad absorption peaks in the region between 1200 cm^{-1} and 1700 cm^{-1} were also observed. Those absorption bands are due to vibrations of carbonates ($ZnCO_3$) [2].

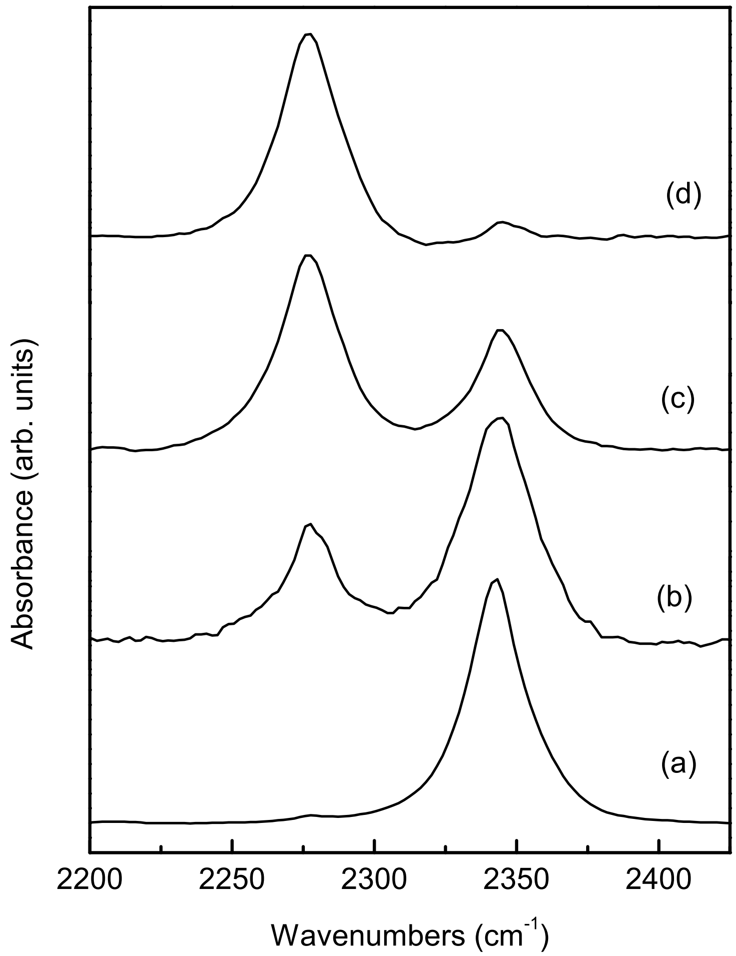

FIG. 4.3. IR absorption spectra of ZnO nanoparticles with different ^{13}C compositions, (see Table. 4.1).

4.2.1 Isotopic substitution

To obtain more conclusive results, the same synthesis procedure was repeated with isotopically enriched precursor materials. Zinc acetate crystals with different ^{13}C compositions were produced by reaction of dilute acetic acid (CH_3COOH) and pure ZnO powder. The detailed compositions and the IR spectra of the precursor materials for each sample are given in Table 4.1, and Fig. 4.4.

TABLE 4.1. Isotopic compositions of precursor materials used to synthesize ZnO nanoparticle samples.

Samples	**Precursor Materials**
Sample(a)	$Zn(CH_3COO)_2$ and $NaHCO_3$ (Natural isotopic abundance)
Sample(b)	$Zn(CH_3COO)_2$ and $NaH^{13}CO_3$
Sample(c)	$Zn(CH_3\,^{13}COO)_2$ and $NaH^{13}CO_3$
Sample(d)	$Zn(^{13}CH_3\,^{13}COO)_2$ and $NaH^{13}CO_3$

IR absorption peaks for each ZnO sample prepared from different precursors are shown in Fig. 4.3. The results indicate that the peak at 2277 cm^{-1} increases with increasing ^{13}C composition in the precursors. Hence, we conclude that the $^{13}CO_2$ molecules originate from the organic precursors. The formation of CO_2 can be explained by a two-step reaction. First, zinc acetate reacts with sodium hydrogen carbonate, producing zinc carbonate and sodium acetate

$$Zn(CH_3COO)_2 + 2\,NaHCO_3 \rightarrow ZnCO_3 + 2\,CH_3COONa + CO_2 + H_2O. \qquad (4.2)$$

The product, zinc carbonate, then decomposes into ZnO and CO_2 by thermal decom-

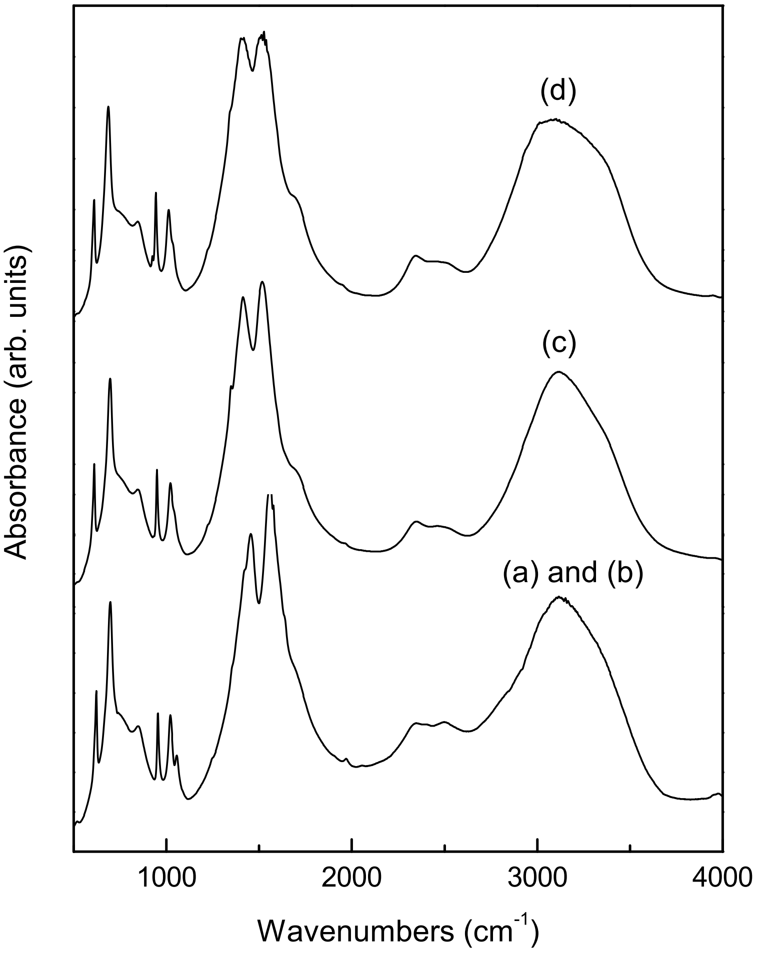

FIG. 4.4. IR absorption spectra of zinc acetate precursors with different ^{13}C compositions (see Table. 4.1).

position

$$ZnCO_3 \rightarrow ZnO + CO_2. \tag{4.3}$$

These reactions account for the observed IR absorption peaks of the carbonates, which remain in the samples (Fig. 4.5). Since zinc carbonate is insoluble in water, one cannot simply remove unreacted zinc carbonate by washing with water. The zinc carbonate therefore remains in the sample and acts as a source of CO_2.

4.3 Stability of CO_2 molecules

To further investigate the stability of CO_2 in nanoparticles, isochronal annealing experiments were performed. The annealing process was carried out in an open-air furnace, over a temperature range of 200 °C to 700 °C. Samples (with natural isotopic abundance) were annealed for a duration of 1 hour at each temperature. IR spectra were taken after each annealing step.

As shown in Figs. 4.5 and 4.6, the intensity of the CO_2 vibrational peak increases with increasing temperature. Correspondingly, the carbonate peaks decrease upon annealing. These observations are in agreement with our model assumption that zinc carbonate is a source of CO_2 impurities.

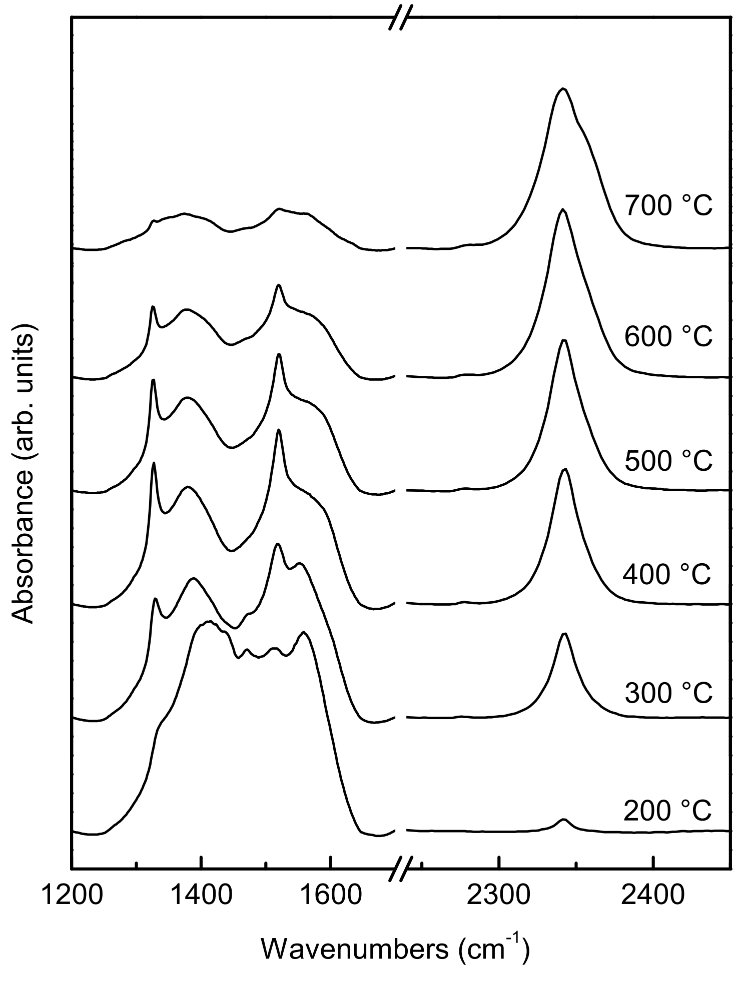

FIG. 4.5. IR absorption spectra of ZnO nanoparticles after each annealing step.

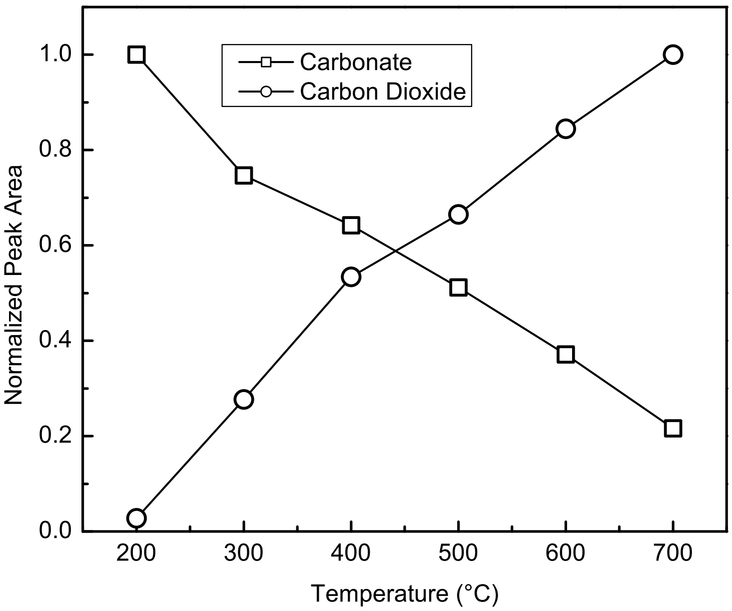

FIG. 4.6. CO_2 and carbonate peak intensities in ZnO nanoparticles after isochronal annealing. Peaks are normalized to their maxima.

4.4 Isotopic exchange reaction

Finally, the possibility of $^{12}CO_2$ contamination from ambient air was investigated. Fig. 4.7 shows IR spectra of samples, with the same ^{13}C composition as sample (d), prepared in air and argon ambients. Despite the absence of ^{12}C atoms in the precursors, a strong absorption peak at 2342 cm^{-1} appeared for the sample prepared in air.

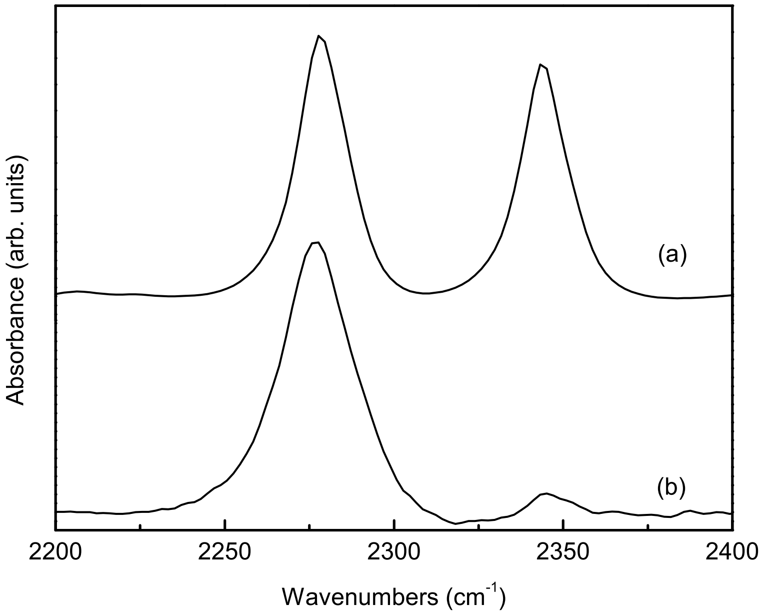

FIG. 4.7. IR absorption spectra of ZnO nanoparticles, (a) prepared in air, (b) prepared in argon gas. The precursors contain only ^{13}C isotopes [sample (d)].

This effect is presumably due to isotope exchange of ^{13}C and ^{12}C during the reaction at 200 °C. Post-growth annealing of sample (d) in $^{12}CO_2$ gas did not result in an increase in the $^{12}CO_2$ peak, indicating that isotope exchange occurs only during the first reaction (Eq. 4.2). During post-growth annealing, therefore, CO_2 molecules are produced only by thermal decomposition of the remaining carbonates in the sample and not from the ambient.

4.5 Bonding of CO_2 molecules to ZnO

To understand the nature of CO_2 bonding to ZnO, we compared our results with those of CO_2 adsorption studies on ZnO surfaces [2,3]. In the adsorption process, CO_2 reacts with ZnO and forms chemical species such as bidentate carbonates, polydentate carbonates, and linear CO_2. The linear molecules, which have vibrational frequencies similar to those of free CO_2, are weakly adsorbed and are not stable. They can be immediately removed by evacuation at room temperature. This observation is different from our results, since CO_2 impurities in our samples are stable even at elevated temperatures.

Interestingly, our results are similar to studies of trapped CO_2 molecules in carbon nanotube bundles, recently reported by Matranga *et al.* [4]. In their work, IR spectroscopy showed that thermal decomposition of oxygen-containing functionalities on carbon nanotubes generated CO_2 molecules that became permanently trapped in the nanotube bundles. The absorption band of trapped CO_2 was centered at 2330 cm^{-1}, which is close to that of the free molecule. They observed that those trapped molecules persist after multiple temperature cycles and are stable for as long as 2 months in a vacuum chamber. These results are qualitatively similar to ours. In the present work, however, it is not known exactly where the CO_2 molecules reside. It is possible, for example, that CO_2 molecules become trapped inside voids in ZnO nanoparticles.

4.6 Conclusions

We have observed the presence of CO_2 impurities in ZnO nanoparticles by IR spectroscopy. Isotopic substitution was used to confirm the vibrational frequency assignment. The CO_2 is formed by thermal decomposition of zinc carbonate, which is a reaction product. The molecules are believed to be trapped within the particles, but their exact location is not known. Further studies on the role of CO_2 impurities on the electrical and optical properties of ZnO nanoparticles will be of considerable practical interest.

References

[1] Z. Wang, H. Zhang, L. Zhang, J. Yuan, S. Yan and C. Wang, Nanotechnology **14**, 11 (2003).

[2] J. H. Taylor and C. H. Amberg, Can. J. Chem. **39**, 535 (1961).

[3] J. Saussey, J. C. Lavalley and C. Bovet, J. Chem. Soc., Faraday Trans. I **78**, 1457 (1982).

[4] C. Matranga, L. Chen, M. Smith, E. Bittner, J. K. Johnson and B. Bockrath, J. Phys. Chem. B, **107**, 12930 (2003).

CHAPTER 5

INFRARED AND RAMAN SPECTROSCOPY OF HYDROGEN ANNEALED ZnO NANOPARTICLES

5.1 Introduction

Infrared reflectance spectroscopy is a useful method to determine free-carrier concentration in semiconductors [1,2]. In the work described in this chapter, we studied the free-carrier concentration in ZnO nanoparticles before and after annealing in hydrogen, using IR reflectance and absorption spectroscopy. Electrical measurements and Raman spectroscopy complemented the IR measurements.

5.2 Literature review

Several IR reflectance spectroscopy studies on ZnO have been performed previously. Collins and Kleinman [3] measured reflectivity of bulk samples in the range between 1 μm and 45 μm. According to their results, for samples with free-carrier concentrations below 10^{16} cm^{-3}, the usual reflection spectrum of an ionic crystal was observed. The

---

Portions of this chapter were published as: W. M. Hlaing Oo, M. D. McCluskey, J. Huso, and L. Bergman, "Infrared and Raman spectroscopy ZnO nanoparticles annealed in hydrogen." *J. Appl. Phys.* **102**, 043529 (2007).

contribution from free carriers becomes significant when the carrier concentration is larger than $\sim 1\times10^{17}$ cm^{-3}. The anisotropy of optical parameters of bulk wurtzite ZnO crystal have also been reported [4,5]. Nan *et al.* [6] measured the IR reflectance spectra of ZnO nanoparticles, which provided evidence of low free-carrier density.

Hydrogen plays an important role in controlling the electrical conductivity of ZnO [7,8]. At nanometer scales, Heo *et al.* [9] demonstrated that post-growth annealing in hydrogen can dramatically increase the conductivity of single ZnO nanorods. In this chapter, evidence for hydrogen donors in ZnO nanoparticles is presented.

5.3 Experimental

The synthesis of ZnO nanoparticles used in this study is similar to that described in chapter 4. The particles were pressed into 7 mm diameter thin pellets. Some of the pellets were sealed in a quartz ampoule filled with 2/3 atm hydrogen and annealed at 350 °C for 1 hour.

Reflectance spectra were taken with a near normal reflectance geometry. The spectral region between 200 cm^{-1} to 500 cm^{-1} were obtained with a Mylar beam splitter and DTGS detector. A KBr beam splitter and MgCdTe detector were used to measure wavenumbers above 500 cm^{-1}. A gold mirror was used as a reference.

Complementary results were obtained by electrical conductivity measurements. A standard 4-probe measurement in the Van der Pauw geometry was used. Electrical contacts were made by conductive silver paint on the periphery of the samples. Resonance Raman spectra of as-grown and hydrogen annealed sample were taken by cw-Kimmon laser with a wavelength 325 nm and a JY-Horiba micro-Raman/PL system. For IR absorption spectra, hydrogen annealed nanoparticles were dispersed in a KBr matrix (1% and 2% wt.), and IR absorption spectra were measured. A pure KBr pellet was used as a reference to minimize the surface scattering effects. To test the effect of ambient gas on the *n*-type conductivity, reflectivity measurements of a hydrogen-annealed sample were performed with a vacuum tight chamber. The sample was placed in the chamber and the desired gas was supplied (1 atm) after the chamber was evacuated. After a 24 hr exposure for each gas, the sample was removed from the chamber and reflectance spectra were recorded. The electrical conductivity measurements were also done in different ambient and the results were recorded as a function of time.

Secondary ion mass spectrometry (SIMS) was performed on an as-grown sample and samples annealed in hydrogen and deuterium at 350 °C for 1 hour. The SIMS measurements used a 14.5 KeV Cs^+ ion beam and an implanted silicon sample for deuterium calibration. The deuterium annealed sample showed a deuterium concentration of 3×10^{20} cm^{-3}. As shown in Fig. 5.1, the deuterium profile was constant down to the maximum depth of the SIMS measurement (8 μm). Although SIMS cannot determine how much hydrogen diffuses into the nanoparticles, our discussion in the next section suggests a doping level in the 10^{19} cm^{-3} range.

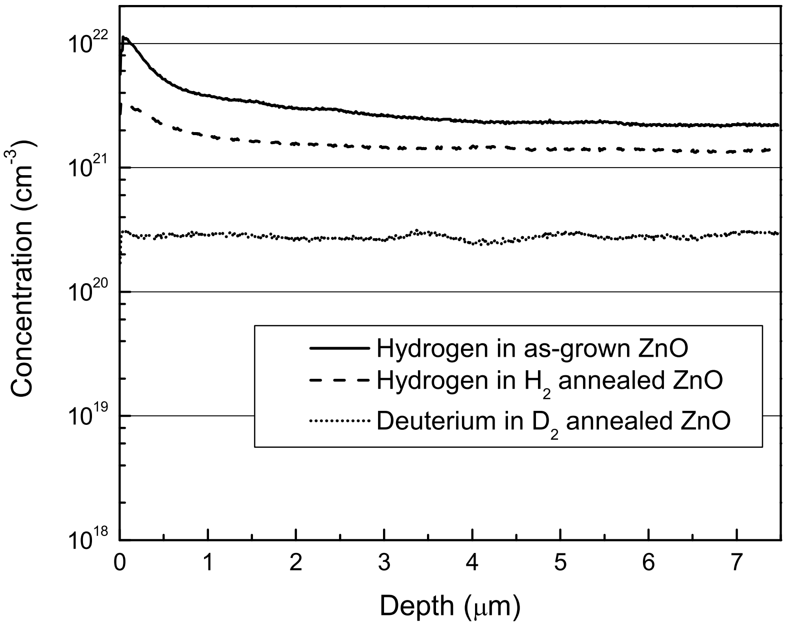

FIG. 5.1. SIMS results for as-grown, H_2 annealed and D_2 annealed ZnO nanoparticles.

5.4 Results and discussion

5.4.1 IR reflectance

Reflectance spectra are shown in Fig. 5.2 for an as-grown sample and a sample annealed in hydrogen. The reflectivity of the as-grown sample shows a sharp decrease in reflectivity ($R_{min} \approx 0$) around the longitudinal optical phonon frequency ω_{LO}. This feature is a typical *reststrahlen* band reflection of semi-insulating ZnO. The hydrogen annealed sample exhibits a change in the *reststrahlen* line shape, and the disappearance of R_{min} was observed. It should be noted that the nanoparticle pellets have a lower overall reflectivity compared that of bulk ZnO, due to open voids in the sample [6]. We repeated the measurements with many different samples to ensure consistency and reproducibility. The electrical measurements showed that the as-grown pellets are semi-insulating ($\rho \sim 10^7$ Ω.cm). Hydrogen annealing reduces the resistivity by several orders of magnitude ($\rho \sim 1$ Ω.cm). This result gives support to the hypothesis that hydrogen annealing leads to an increase in free-carrier concentration. Annealing in air or argon gas does not result in any changes in the reflectivity or conductivity.

5.4.2 Modeling

To model the reflectance spectra, we used the Lorentz-Drude model (Eq. 3.28) and Fresnel's equation (Eq. 3.7). The previous expressions are applicable for bulk surfaces, but do not produce satisfactory results for nanoparticle pellets. In nanoparticles, the existence of one free electron in a 20 nm diameter particle yields a free-carrier concentration of $\sim 2 \times 10^{17}$ cm^{-3}. Since the as-grown sample is semi-insulating, we assumed that some fraction of the particles have no free carrier ($n = 0$), and the remaining particles have one electron each ($\sim 2 \times 10^{17}$ cm^{-3}). For the hydrogen annealed sample, an additional constituent of heavily doped particles (10^{19} cm^{-3}) was included. This assumption is to simplify the model; in fact, the inhomogeneity of dopants among the nanoparticles is typically described by a binomial distribution [10]. The dielectric functions for each ZnO constituent were calculated using Eq. 3.28 with different free-carrier concentrations, and the open voids were taken as $\varepsilon = 1$.

The effective dielectric function ε_{eff} for an inhomogeneous medium is given by the Bruggeman model (Eq. 3.41), and the reflectance spectra were modeled by Eq. 3.7 with the calculated values for ε_{eff}. The surface roughness correction was applied by Eq. 3.29. The rms value of the roughness δ was chosen as an adjustable parameter; δ=47 nm was used in all fits.

The simulated spectra and parameters used in the fits are presented in Fig. 5.2 and Table 5.1, respectively. Small discrepancies between the models and experiments are due, in part, to the anisotropy of phonon frequencies and our simplified model of inhomogeneity. Nevertheless, the model is in good agreement with measured spectra and it suggests that the nanoparticles have an inhomogeneous free-carrier concentration.

Due to their large surface-to-volume ratio, nanoparticles are susceptible to contamination from the ambient. Fig. 5.3 shows reflectance spectra of a hydrogen-annealed sample, measured after the sample was exposed to air. The fits to the IR spectra indicate that the drop in reflectivity is due to a reduction in the fraction of heavily

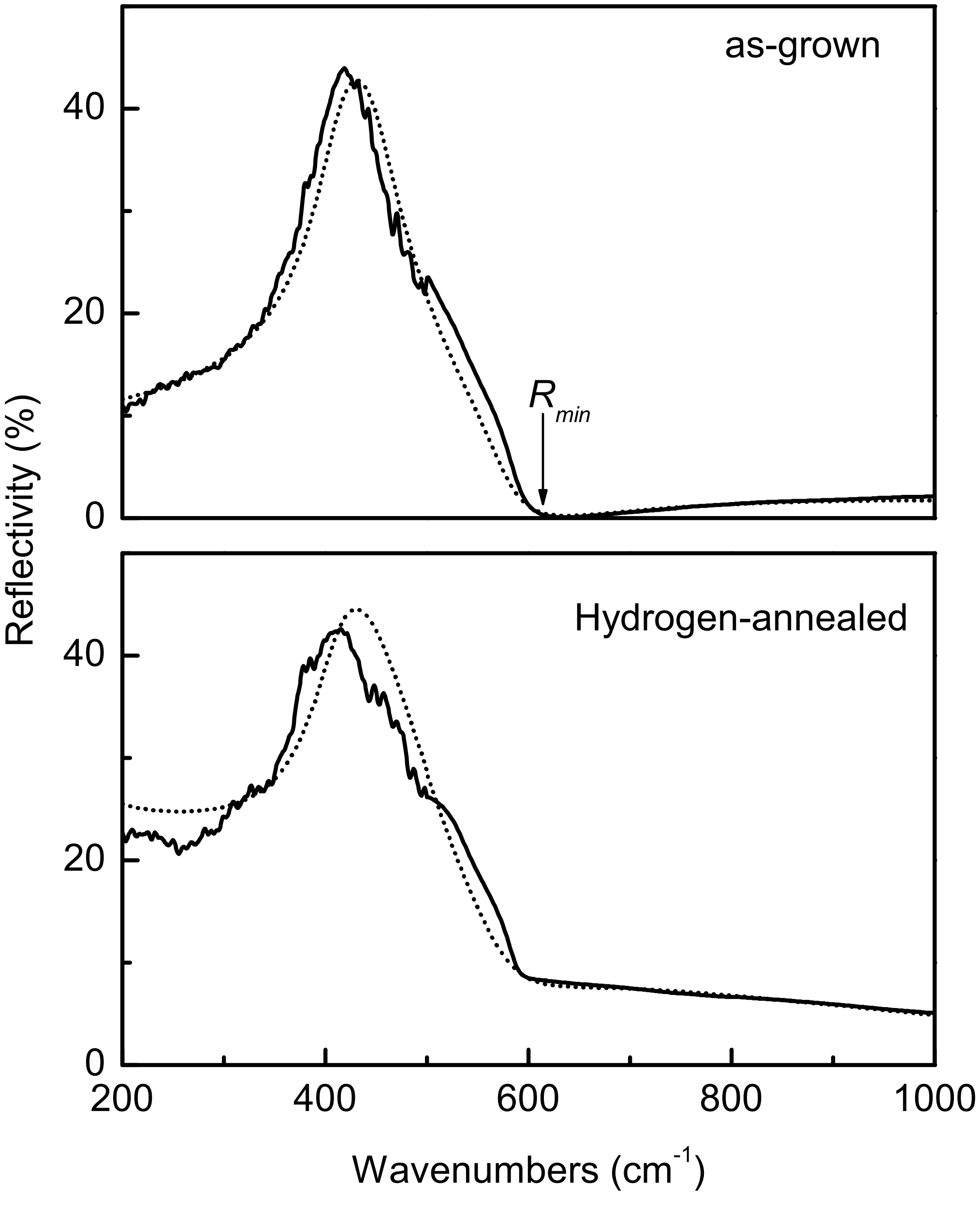

FIG. 5.2. Infrared reflectance spectra of ZnO nanoparticles. The dotted lines denote the calculated spectra.

TABLE 5.1. Parameters used in the calculations. Constants are: $\omega_{\mathrm{TO}} = 410$ cm^{-1}, $\omega_{\mathrm{LO}} = 575$ cm^{-1}, and $\varepsilon_\infty = 3.75$.

Sample	f(%)	ω_p (cm^{-1})	n(cm^{-3})	γ (cm^{-1})	Γ (cm^{-1})
As-grown	30	0	0	-	50
	31	160	2×10^{17}	150	50
Hydrogen-annealed	32	230	6×10^{17}	150	65
	29	1900	4×10^{19}	1350	60
After 1 days	34	230	6×10^{17}	150	65
	27	1800	3.6×10^{19}	1350	60
After 21 days	35	230	6×10^{17}	150	60
	26	1700	3.2×10^{17}	1350	60
in KBr matrix (1% wt.)	0.25	230	6×10^{17}	150	65
	0.275	1900	4×10^{19}	2550	60
in KBr matrix (2% wt.)	0.5	230	6×10^{17}	150	65
	0.44	1900	4×10^{19}	2550	60

doped particles (Table 5.1). It is possible that oxygen in ambient air could capture the free carriers in the nanoparticles. Nanoparticles have a large surface-to-volume ratio, and oxygen molecules can be adsorbed on the surfaces as negatively charged ions. The adsorbed oxygen molecules transform n-type nanoparticles to a semiconducting phase. To test this hypothesis, we investigated the stability of IR reflectivity under different ambients. As shown in Fig. 5.4, exposure to oxygen gas results the largest drop in the reflectivity. Small changes in the other the spectra may be due to adsorption of oxygen from the air as the sample was transferred between the gas chamber and the spectrometer.

Raman spectra of as-grown and hydrogenated ZnO nanoparticles are shown in Fig. 5.5. Unlike bulk ZnO [11], LO phonon-plasmon coupling (LOPC) does not broaden the LO phonon line shape of the doped sample. This may due to the fact

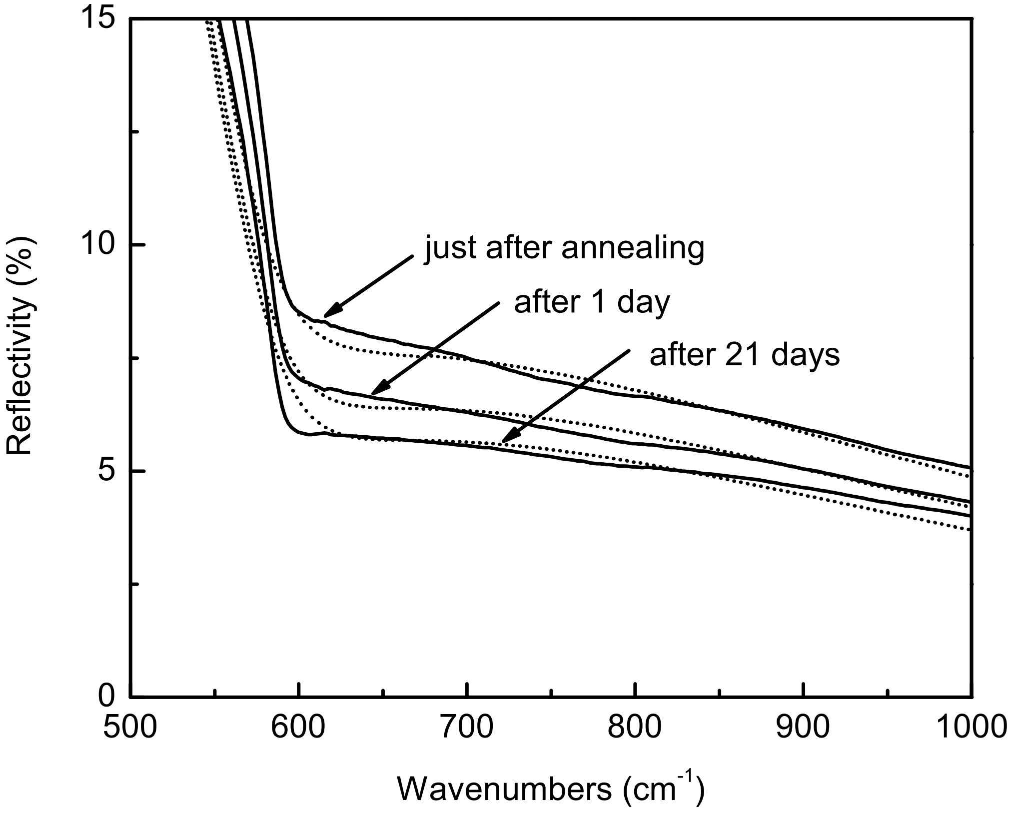

FIG. 5.3. Infrared reflectance spectra of hydrogen annealed ZnO nanoparticles after exposure to air. The dotted lines denote the calculated spectra.

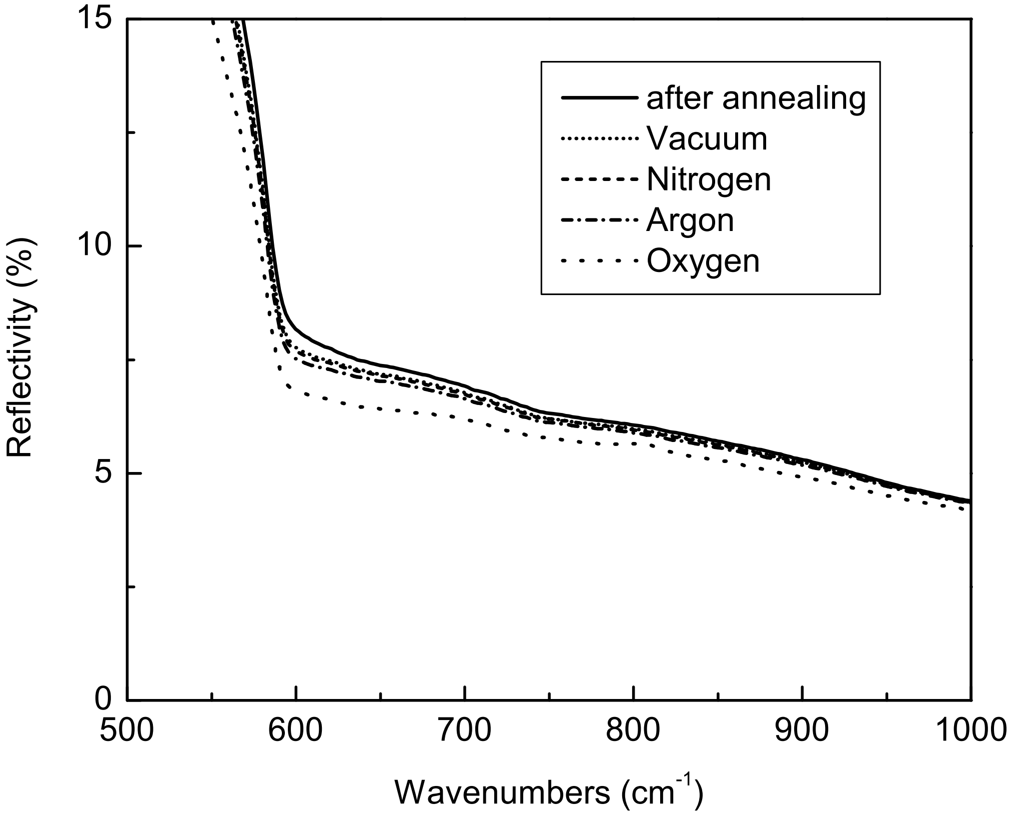

FIG. 5.4. IR reflectance spectra of hydrogen-annealed sample, under different ambients.

that a significant fraction of the nanoparticles are not heavily doped. In addition, it is conceivable that the LOPC strength is lower in nanoparticles than in bulk crystals. Another possibility is that LOPC does not show in resonance Raman spectra (we have not performed at non-resonance Raman measurements). A recent report [12] shows that a broadening of the LO phonon was found in non-resonance Raman spectra of hydrogen-annealed ZnO powder.

We also measured the IR transmittance of a hydrogen-annealed sample to detect hydrogen local vibrational modes. Unfortunately, the sample was opaque to IR radiation in the spectral range of interest (Fig. 5.6). Similar difficulties were also encountered in hydrogen plasma treated ZnO thin films [13]. To address that problem, we mixed small quantities of ZnO in a KBr pellet.

5.4.3 IR absorption of hydrogen annealed ZnO nanoparticles

IR absorption spectra (Fig. 5.7) of hydrogen nanoparticles in a KBr matrix show characteristic free-carrier absorption, as absorption increases with wavelength. To model the absorption spectra, the modified Maxwell-Garnett (MG) model [15] was chosen, which is appropriate for dilute quantities of ZnO in a KBr host. The effective dielectric function is given by

$$\varepsilon_{\mathrm{eff}} = \varepsilon_{\mathrm{KBr}} \left(\frac{3 + 2\sum_j f_j p_j}{3 - \sum_j f_j p_j} \right), \tag{5.1}$$

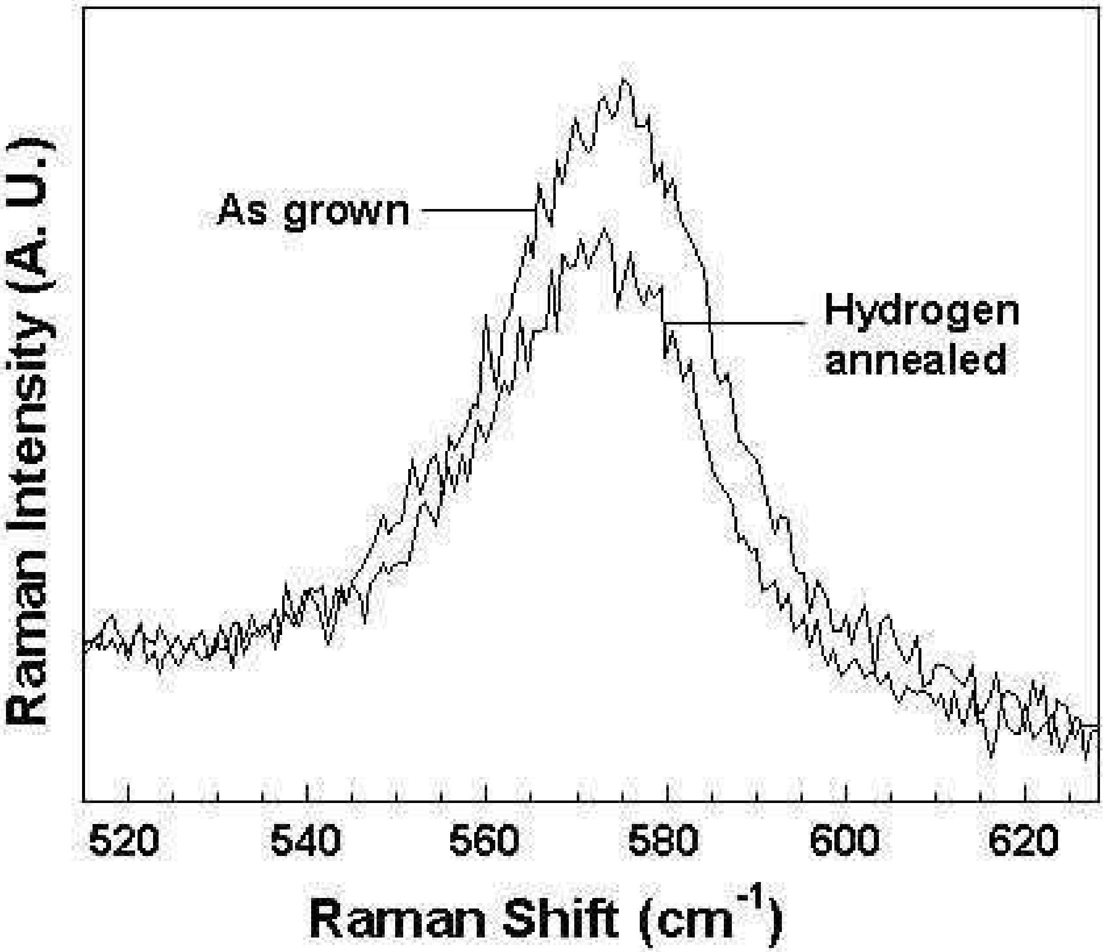

FIG. 5.5. Raman spectra of ZnO nanoparticles.

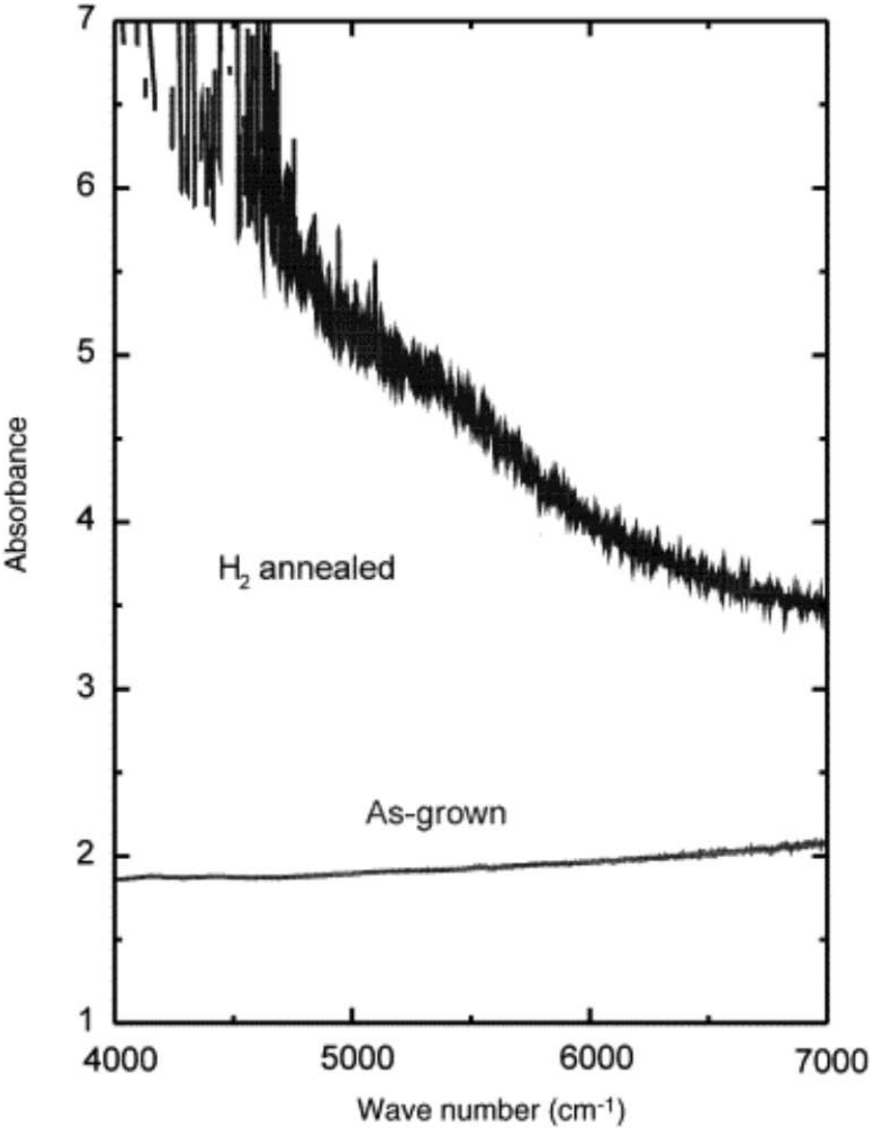

FIG. 5.6. Free-carrier absorption of ZnO nanoparticles, as-grown and after annealing in hydrogen at 350 °C (from Ref. [8]).

where

$$p_j = 3\left(\frac{\varepsilon_j - \varepsilon_{\mathrm{KBr}}}{\varepsilon_j + 2\varepsilon_{\mathrm{KBr}}}\right). \tag{5.2}$$

The similar procedure described previously was used to calculate the dielectric function of ZnO nanoparticles (ε_j). The dielectric constant for KBr was taken as $\varepsilon_{\mathrm{KBr}}$=2.34. The absorption coefficient α was determined by Eq. 3.35. The calculated absorption spectra show good agreement with the measured spectra (Fig. 5.7). The estimated plasma frequencies for the reflectance and absorption spectra are also in good agreement (Table 5.1).

Although hydrogen clearly affects the conductivity of ZnO nanoparticles, we were unable to detect hydrogen related local vibrational modes (LVMs). The reason for this null result may be that IR absorption peaks are broad such that the signal is below the noise. Alternatively, hydrogen may modify the nanoparticle and then desorb, resulting in an n-type defect such as an oxygen vacancy.

5.4.4 Conductivity under different ambients.

In contrast to the IR reflectivity results, the electrical conductivity of hydrogen-annealed samples drops in all ambient conditions (Fig. 5.8). One possible reason is that the conductivity of a pellet is dominated by grain boundaries, which is not an issue in IR reflectivity. While the conductivity under vacuum is more stable than other gases, it is difficult to correlate the reflectivity and conductivity results.

The effect of ambient pressure on conductivity can be seen clearly in Fig. 5.9. A rapid change in conductivity was observed when the ambient air was allowed to interact

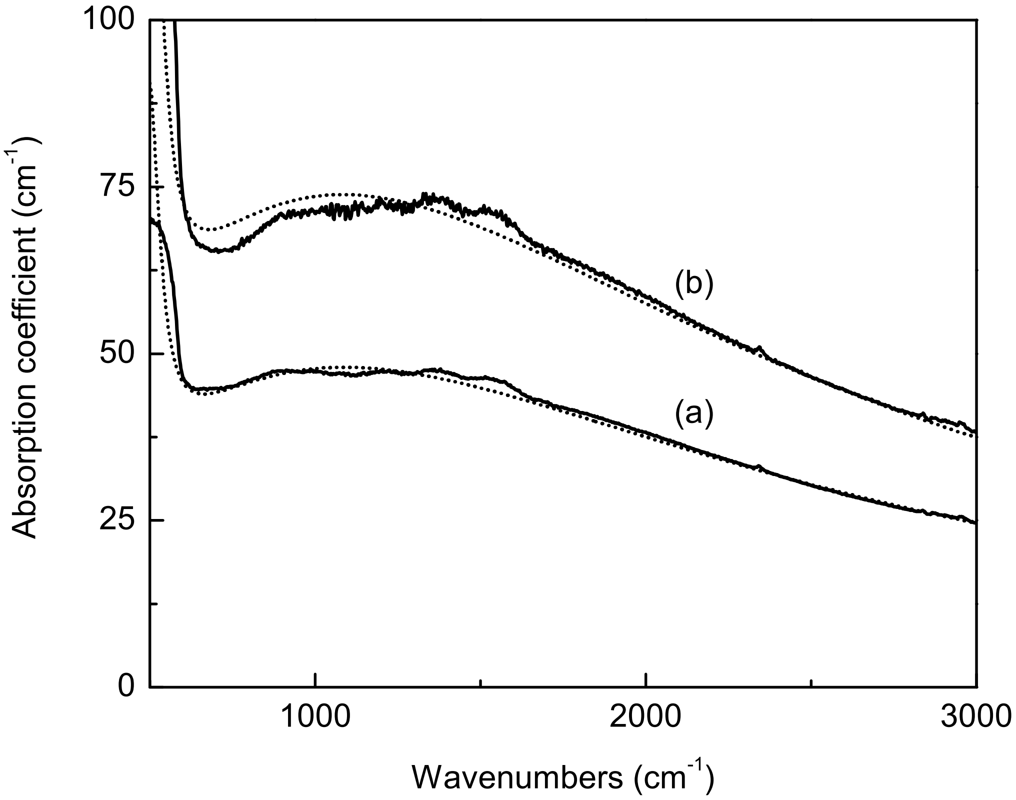

FIG. 5.7. Infrared absorption spectra of hydrogen annealed ZnO nanoparticles in KBr matrix (a) 1% wt. and (b) 2% wt. The dotted lines represent the model.

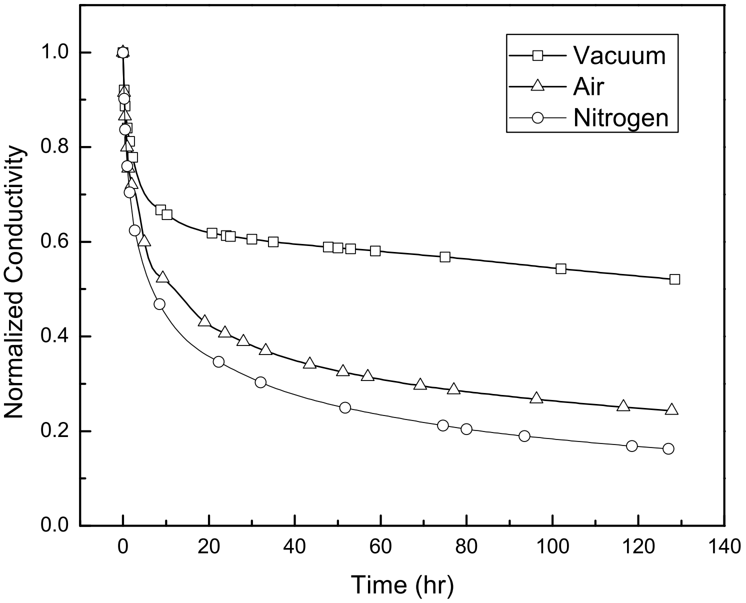

FIG. 5.8. Conductivity under different ambients.

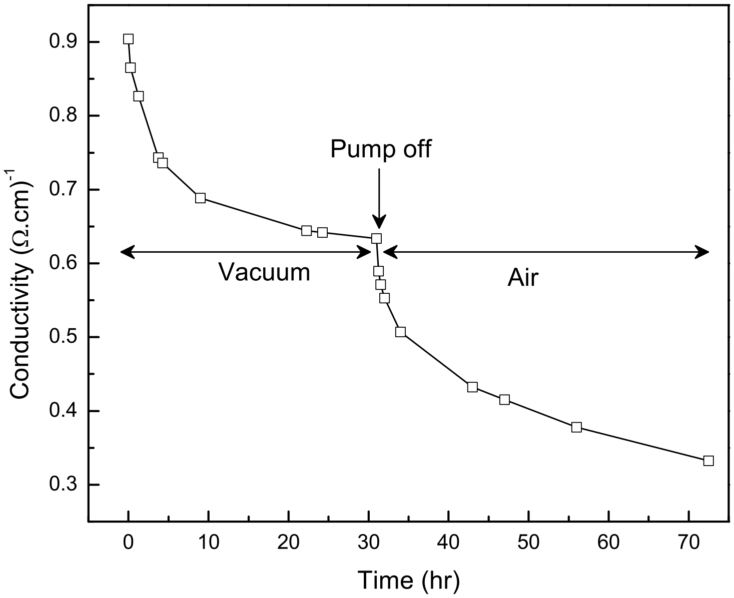

FIG. 5.9. Conductivity under vacuum and air ambient.

with the sample. A similar result was also observed in nitrogen gas (Fig. 5.10).

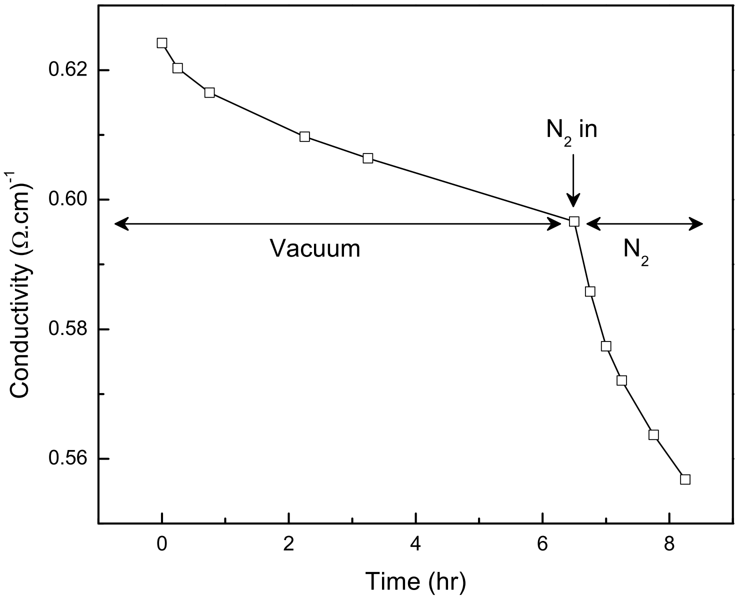

FIG. 5.10. Conductivity under vacuum and nitrogen ambient.

5.5 Conclusions

We demonstrated the effect of hydrogen annealing on ZnO nanoparticles. IR reflectance and absorption spectra indicate that hydrogen significantly increases the free-carrier concentration. The spectra were modeled using the effective medium approximation, given an inhomogeneous free-carrier concentration. The large surface area of nanoparticles provides adsorption sites for oxygen molecules that can capture electrons and reduce the free-electron concentration. Although the IR reflectance spectra show significant differences between as-grown and hydrogen annealed samples, Raman results do not show a statistically significant difference. These results indicate that IR spectroscopy may provide a superior method for determining the doping level in ZnO nanoparticles.

References

[1] T. S. Moss, T. D. Hawkins and G. J. Burrell, J. Phys. C: Solid State Phys. **1**, 1435 (1968).

[2] W. Songprakob, R. Zallen, W. K. Liu and K. L. Bacher, Phys. Rev. B **62**, 4501 (2000).

[3] R. J. Collins and D. A. Kleinman, J. Phys. Chem. Solids **11**, 190 (1959).

[4] E. C. Helmetes, and H. L. Swinney, J. Appl. Phys. **38**, 2387 (1967).

[5] E. F. Venger, A. V. Melnichuk, L. Y. Melnichuk and Y. A. Pasechnik, Phys. Stat. Sol. (b) **188**, 823 (1995).

[6] C. Nan, R. Birringer, W. Krauss, Haibin Gao , and H. Gleiter, Phys. Stat. Sol. (a) **162**, R3 (1997).

[7] C. G. Van de Walle, Phys. Rev. Lett. **85**, 1012 (2000).

[8] M. D. McCluskey, S. J. Jokela, K. K. Zhuralev, P. J. Simpson, and K. G. Lynn, Appl. Phys. Lett. **81**, 3807 (2002).

[9] Y. W. Heo, L. C. Tien, D. P. Norton, B. S. Kang, F. Ren , B. P. Gila and S. J. Pearton, Appl. Phys. Lett. **85**, 2002 (2004).

[10] J. D. Bryan and D. R. Gamelin, Progress in Inorganic Chemistry **54**, 74 (2005).

[11] B. H. Bairamov, A. Heinrich, G. Iremer, V. V. Toporov, and E. Ziegler, Phys. Stat. Sol. (b) **119**, 227 (1983).

[12] C. F. Windisch, G. J. Exarhos, C. Yao, and L. Wang, J. Appl. Phys. **101**, 123711 (2007).

[13] C. A. Wolden, T. M. Barnes, J. B. Baxter and E. S. Aydil, J. Appl. Phys. **97**, 043522 (2005).

[14] M. D. McCluskey, S. J. Jokela and W. M. Hlaing Oo, Physica B **376-377**, 690 (2006).

[15] C. G. Granqvist and O. Hundrei, Phys. Rev. B **16**, 3513 (1977).

CHAPTER 6

INFRARED SPECTROSCOPY OF COPPER DOPED ZnO NANOPARTICLES.

Copper impurities play an important roles in the optical and electrical properties of ZnO. In this work, I present the IR optical transition spectra of Cu ions in ZnO nanoparticles.

6.1 Copper impurities in ZnO

Copper, a $3d$ transition metal, is incorporated into the ZnO lattice by substituting Zn sites. The substitution leads the Cu impurity to assume the charge state of Cu^{2+} ($3d^9 4s^2$). The Cu^{2+} ion can also capture an extra electron and transform to the Cu^{+} ($3d^{10} 4s^2$) state. The electronic states of Cu^{2+} ions can be described by crystal field splitting. When an impurity atom is placed within the crystal field of surrounding atoms, the energy levels of the atom are perturbed by the crystal field, resulting in the splitting of degenerate states. In a cubic tetrahedral field, the d electron orbital splits into an upper ^2T and lower ^2E states (Fig. 6.1). Both ^2T and ^2E states are located just below the conduction band; thus, the Cu^{2+} impurity acts as a deep acceptor.

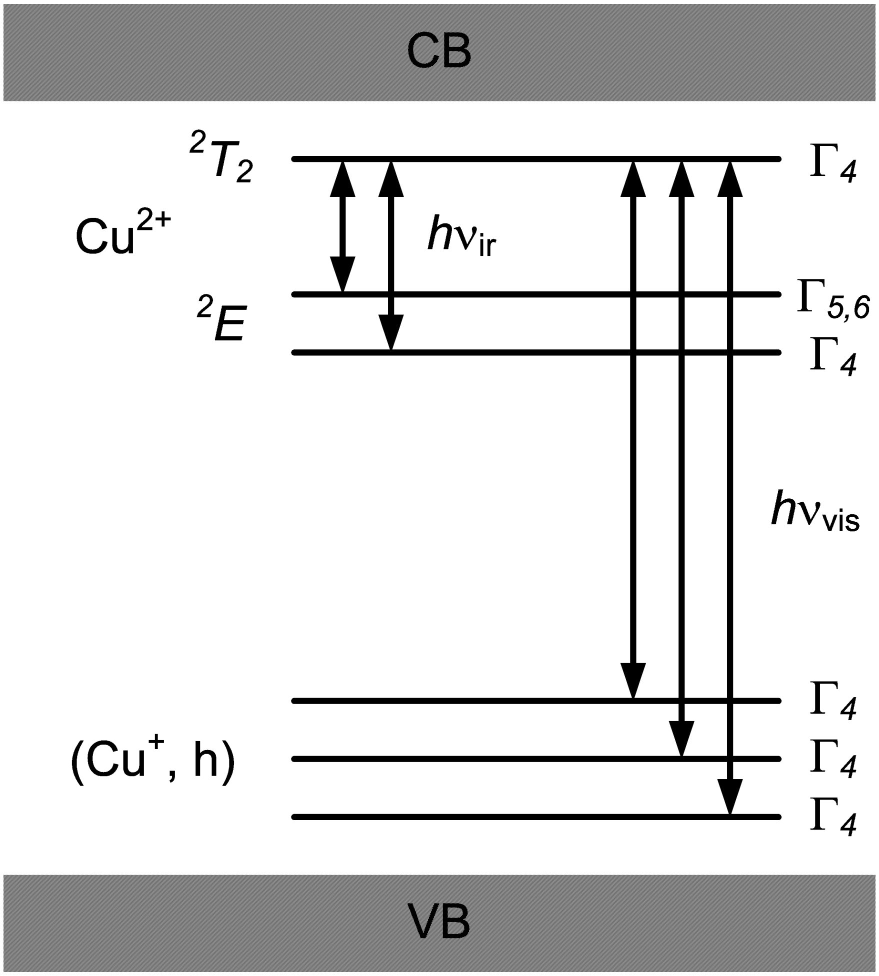

FIG. 6.1. Energy states of Cu in ZnO. From Ref. [1]

6.2 Experimental

A similar procedure to that described in Chapter 4 was used to synthesize Cu doped ZnO nanoparticles. Instead of using pure zinc acetate, a Cu doped zinc acetate precursor was used. For the precursor preparation, 9.0 g of $Zn(CH_3COO_2) \cdot 2\,H_2O$ was dissolved in 20 ml of water at 80 °C, and 0.07 g of $Cu(CH_2COO)_2$ was added. The solution was cooled down to room temperature and kept for 1 day to allow the crystal to grow. Then, the crystals were collected and dried at room temperature. Using this precursor, nanoparticles were grown. The as-grown ZnO:Cu nanoparticles show a faint greenish color.

The ZnO:Cu powder was pressed into a thin pellet to measure the IR spectrum. The sample was mounted inside a liquid helium cooled cryostat and the IR spectrum was taken at 9 K. A Ge:Cu detector was used. The spectrum was averaged over 500 scans and the spectral resolution was 1 cm^{-1}.

6.3 Results

The IR absorption spectrum is presented in Fig. 6.2. Two absorption peaks were observed at energies of 5781 cm^{-1} and 5821 cm^{-1}. These absorption peaks arise from internal transitions of Cu^{2+} ions between the ^2T state and two sublevels of the ^2E state. Similar absorption lines were also observed in bulk ZnO [2,3]. The width of the absorption peaks in our nanoparticles are broader than that of bulk crystals.

In some samples, a series of unidentified peaks were also observed in the region of 3500-3800 cm^{-1} (Fig. 6.3). Those peaks were found only in Cu-doped samples. Samples that showed a high degree of residual water contamination, however, did not show these peaks. We note that absorption peaks related to CuO and Cu_2O phases were not observed, indicating that the nanoparticles were free from copper oxide phases.

We measured the electrical resistivity of ZnO:Cu nanoparticle pellets and unfortunately reliable results were not obtainable. The typical resistivity of undoped ZnO nanoparticle pellet is $\sim 10^7$ Ω.cm (see Ch. 5), and Cu doped particles are likely to have even lower free carrier concentrations than undoped particles. That property is similar to bulk samples in which *n*-type dopants are compensated by Cu acceptors.

6.4 Conclusions

We showed that ZnO nanoparticles can be doped with Cu by using a Cu-doped zinc acetate precursor. The electronic transitions of Cu^{2+} ions were observed in the IR absorption spectrum at low temperatures, which is an evidence of Cu substitution for Zn atoms. The high resistivity property indicates that the copper deep acceptor could capture a free electron from conduction band. We plan to investigate this topic further, starting in January 2008.

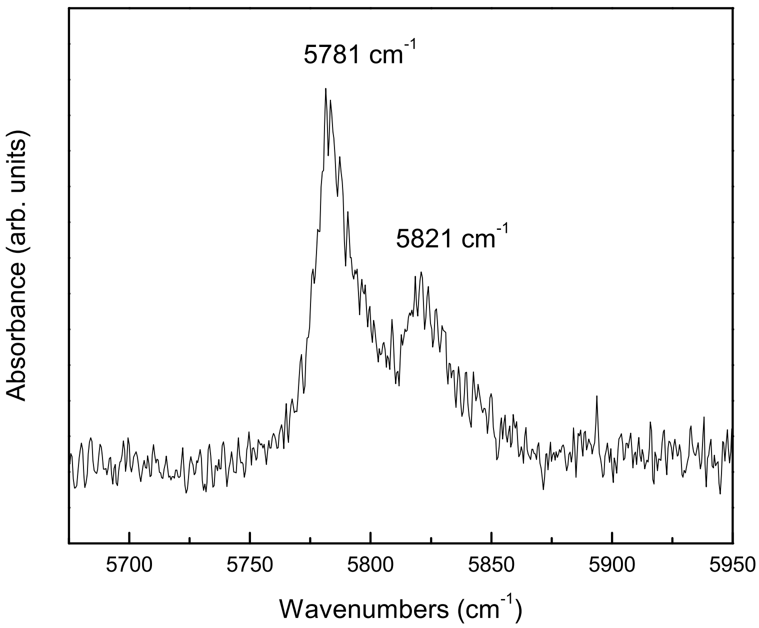

FIG. 6.2. IR absorption spectrum of ZnO:Cu nanoparticles at 9 K.

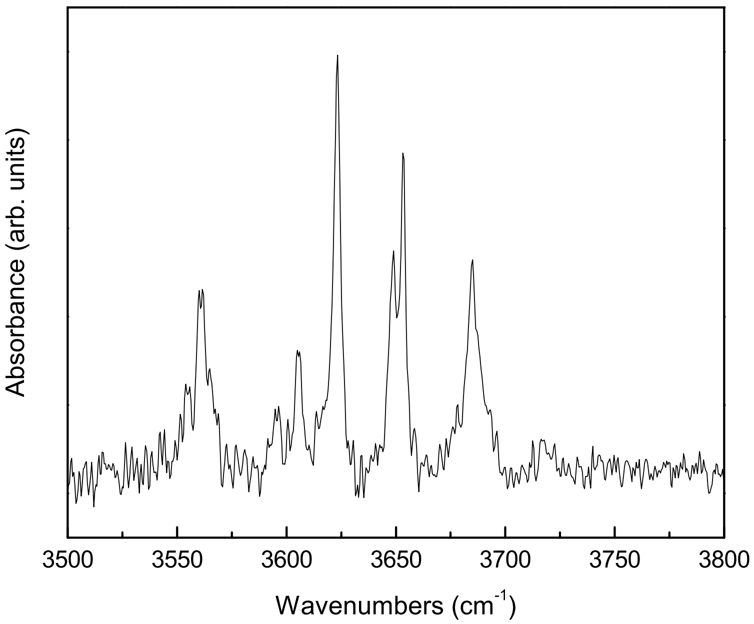

FIG. 6.3. IR absorption spectrum of ZnO:Cu nanoparticles at 9 K (3500-3800 cm^{-1} region)

References

[1] P. Dahan, V. Fleurovy, P. Thurianz, R. Heitzz, A. Hoffmannz, and I. Broserz, J. Phys. Condens. Matter **10**, 2007 (1998).

[2] R. E. Dietz, H. Kamimura, M. D. Struge, and A. Yariv, Phys. Rev. **132**, 1559 (1963).

[3] N. Y. Garces, L. Wang, L. Bai, N. C. Giles, L. E. Halliburton, and G. Cantwell, Appl. Phys. Lett. **81**, 622 (2002).

CHAPTER 7

INFRARED SPECTROSCOPY OF OXYGEN-HYDROGEN BONDS ON MAGNESIUM NANOSTRUCTURES: THE FANO EFFECT

The Fano effect, observed for absorption peaks of hydroxide molecules on metallic magnesium nanorods, is presented in this chapter. Non-metallic magnesium hydride, in contrast, does not exhibit the Fano effect.

7.1 Fano resonance

The Fano resonance, investigated by Ugo Fano [1], describes the quantum mechanical coupling of a discrete energy state with a continuum of states (Fig. 7.1). The coupling leads to a characteristic asymmetric line shape in the optical response.

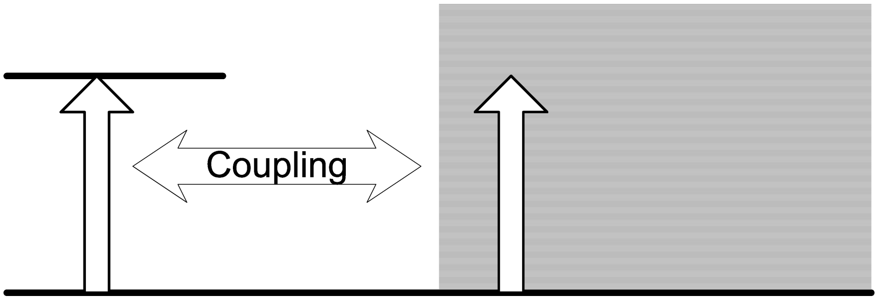

FIG. 7.1. Fano resonance.

The superposition of a discrete state $|\varphi\rangle$ and continuum state $|\psi_{E'}\rangle$ can be written as

$$\Psi_E = a_\varphi|\varphi\rangle + \int b_{E'}|\psi_{E'}\rangle dE'. \tag{7.1}$$

The transition probabilities from the initial state $|i\rangle$ to the perturbed $|\Psi_E\rangle$ and unperturbed $|\psi_E >$ continuum states are $\langle\Psi_E|T|i\rangle$ and $\langle\psi_E|T|i\rangle$ respectively. The Fano line shape is given by the ratio of the two transition probabilities,

$$\frac{\langle\Psi_E|T|i\rangle}{\langle\psi_E|T|i\rangle} = \frac{(q+\varepsilon)^2}{1+\varepsilon^2}. \tag{7.2}$$

The variable ε is defined as a reduced energy:

$$\varepsilon = \frac{2(E-E_0)}{\Gamma}, \tag{7.3}$$

where E_0 is the resonance energy with a width Γ.

Detailed derivations of the Fano function can be found in Refs. [1,2]. The parameter q is the asymmetry parameter, which determines the asymmetric feature of the peak line shape and hence the degree of coupling. The Fano line shape approaches a symmetric Lorentzian shape as $q \rightarrow \infty$. Plots of the Fano line shape with different q values are presented in Fig. 7.2.

Although the theory was initially developed for autoionization of atoms, the Fano effect has been observed in a wide range of areas such as IR absorption lines of adsorbates on thin metal films [3], Raman line shapes [4,5], and local vibrational modes

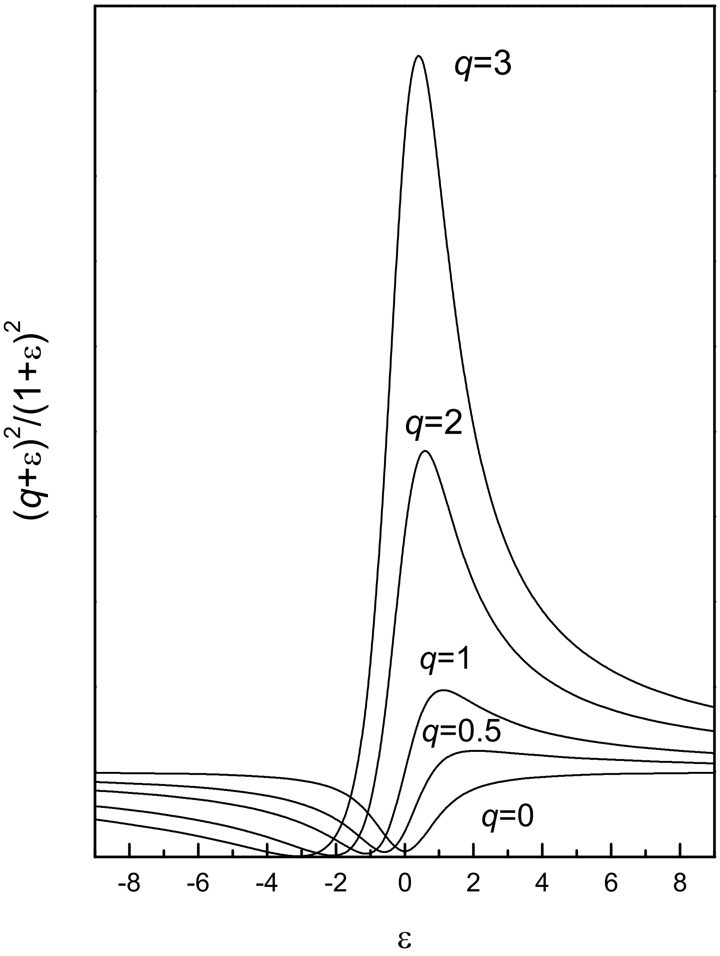

FIG. 7.2. Fano line shape with different q values.

(LVMs) in heavily doped semiconductors [6,7].

7.2 Fabrication of magnesium nanorods

The Mg nanorods [1] were fabricated by the glancing angle deposition (GLAD) technique [8]. The sample fabrication was performed in a high vacuum chamber with a background pressure of 3×10^{-7} Torr. The Mg (99.95 %, from CERAC, Inc.) source was evaporated by electron beam bombardment. The pressure during deposition was less than 1×10^{-6} Torr, and the growth rate was monitored by a quartz crystal microbalance (QCM) and was fixed at 0.5 nm/s. The incident angle of vapor flux with respect to the substrate normal was fixed at 86°. The distance between the evaporation source and the substrate was approximately 20 inches. Using these deposition parameters, a layer of Mg nanorods with a nominal thickness (QCM reading) of 4 mm was grown on Si (100) substrate. A scanning electron microscope (SEM) image of Mg nanorods is shown in Fig. 7.3.

7.3 Experimental

The magnesium nanorods sample was reacted with a boiling H_2O-D_2O mixture for 5 min, and dried in the air at 150 °C for 5 min. IR spectra were taken at room temperature. The spectral resolution was 4 cm^{-1} and the spectra were averaged over 500 scans. A KBr beam splitter and liquid nitrogen cooled MgCdTe detector were used. The spectrum from a plain silicon substrate was used as a reference to calculate

---

[1] Mg nanorods and SEM image were provided by Prof. Yiping Zhao's group (University of Georgia).

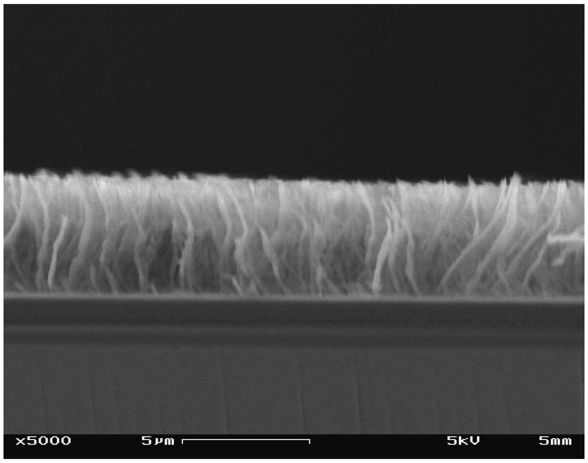

FIG. 7.3. SEM image of Mg nanorods on a Si substrate.

the absorbance spectra.

A similar procedure was performed to produce $Mg(OH)_2$ from commercial Mg and MgH_2 powder. The materials were obtained from Sigma-Aldrich and experiments were done without further purification. The powder samples were diluted with KBr powder and pressed into thin pellets to measure IR absorption. The IR spectrum of a pure KBr pellet was used as a reference. An X-ray diffraction (XRD) spectrum of Mg powder after reaction with water was taken to determine whether bulk $Mg(OH)_2$ was formed.

7.4 Results and discussions

Absorption peaks at 3699 cm^{-1} and 2712 cm^{-1} were observed (Fig. 7.4) and assigned as vibrational frequency of OH and OD from the magnesium hydroxide compounds [9]. The asymmetric line shape feature was observed in both OH and OD absorption peaks. The appearance of a Fano line shape in Mg samples is due to coupling of vibrations of hydroxide molecules and continuum states of metallic magnesium.

In Fig. 7.4, an asymmetric line shape feature was observed in the Mg powder sample, similar to that of Mg nanorods samples. Broad absorption peaks were present on the shoulder of the peaks, perhaps due to water contaminants in the KBr powder. We also observed that the OH vibrational peaks are broader than OD peaks. Thus, we used OD vibrational peaks for the Fano analysis.

The OD vibrational peak in MgH_2 sample, in contrast to the Mg samples, exhibits a symmetric line shape. A single Gaussian curve fit is presented in Fig. 7.5. The symmetric line shape indicates the lack of the Fano effect. Since magnesium hydride is an insulator ($\sim$5.6 eV bandgap [10,11]), it does not have a continuum to interact with the OD vibrational mode.

The Fano line shapes of OD absorption peaks in Mg samples were characterized by the Fano formula. In addition, a Lorentzian function was used to model the weak peak on the low-energy side. The least-squares fits lead to line shape parameters of q=-3.48 and -5.76 for the nanorods sample and powder sample, respectively (Fig. 7.6). The values of q suggest that the coupling is stronger in the nanostructured sample than that of the powder sample. Slight variations in resonance frequency ω_0 and peak width Γ were also observed.

Li et al. [12] reported that a Fano-like peak of adsorbed CO species was observed only on nanostructured Pt microelectrodes, whereas a normal peak was observed on bulk structures. This observation is similar to our results. It is possible that nanostructured substrates could enhance the coupling between the adsorbates and the metal.

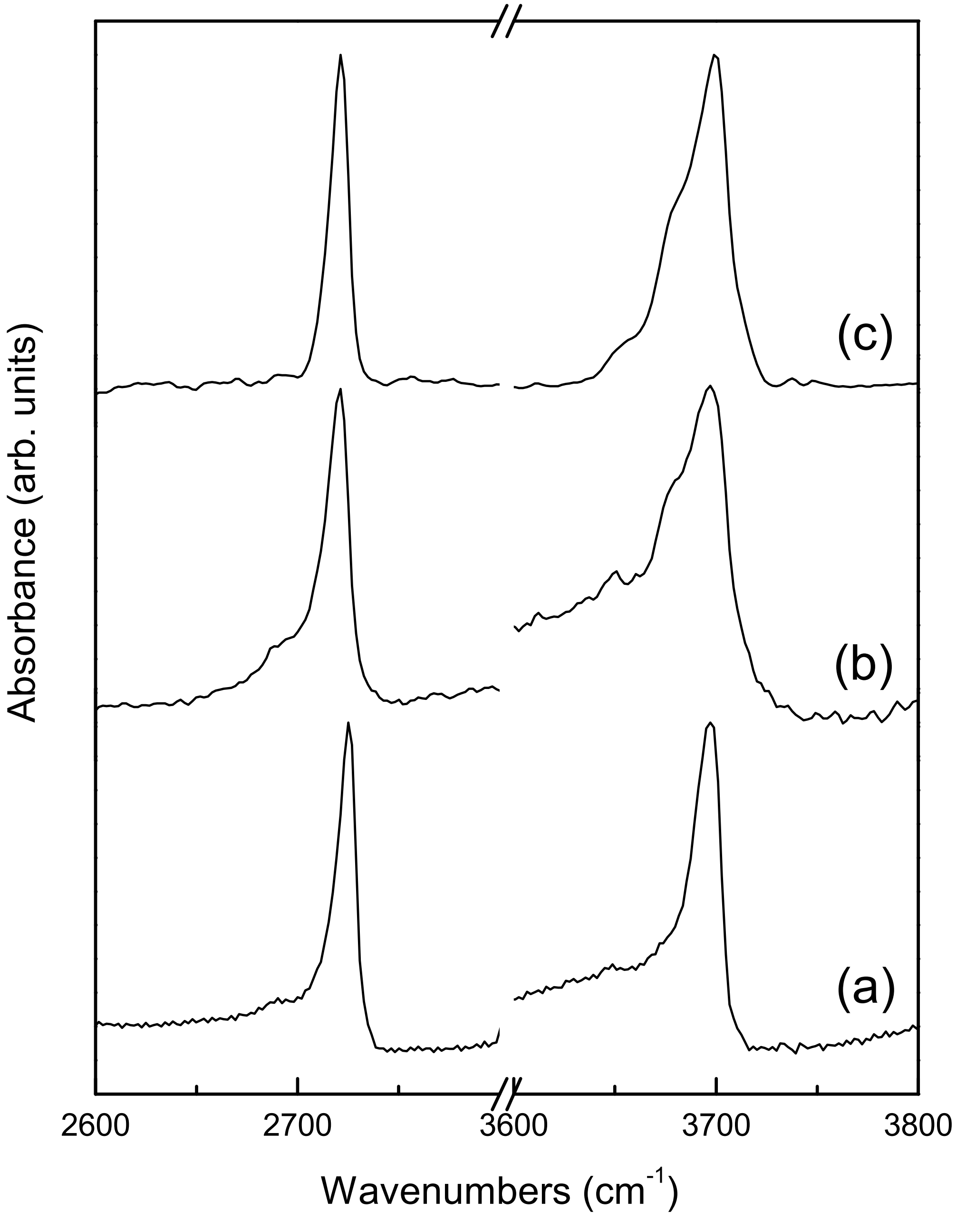

FIG. 7.4. OH and OD absorption peaks on (a) Mg nanorods, (b) Mg powder, and (c) MgH_2 powder.

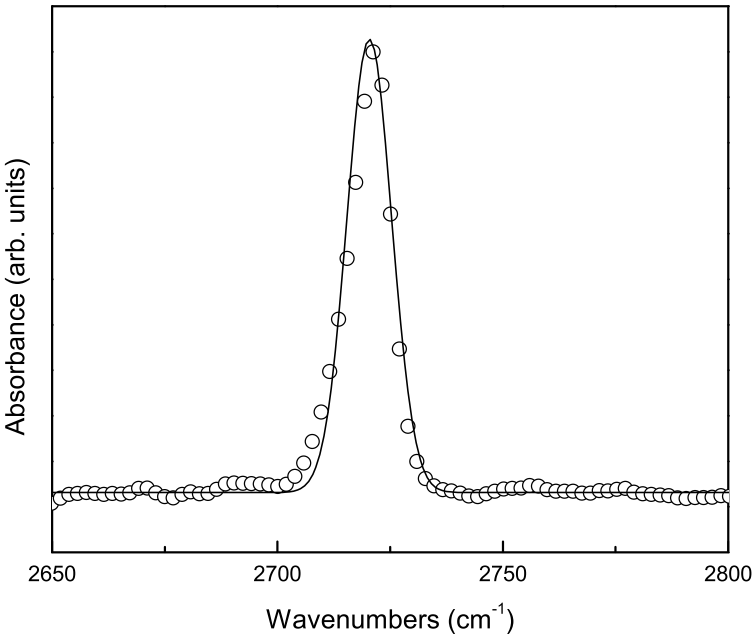

FIG. 7.5. Gaussian line shape fit of OD absorption peak in the MgH_2 sample.

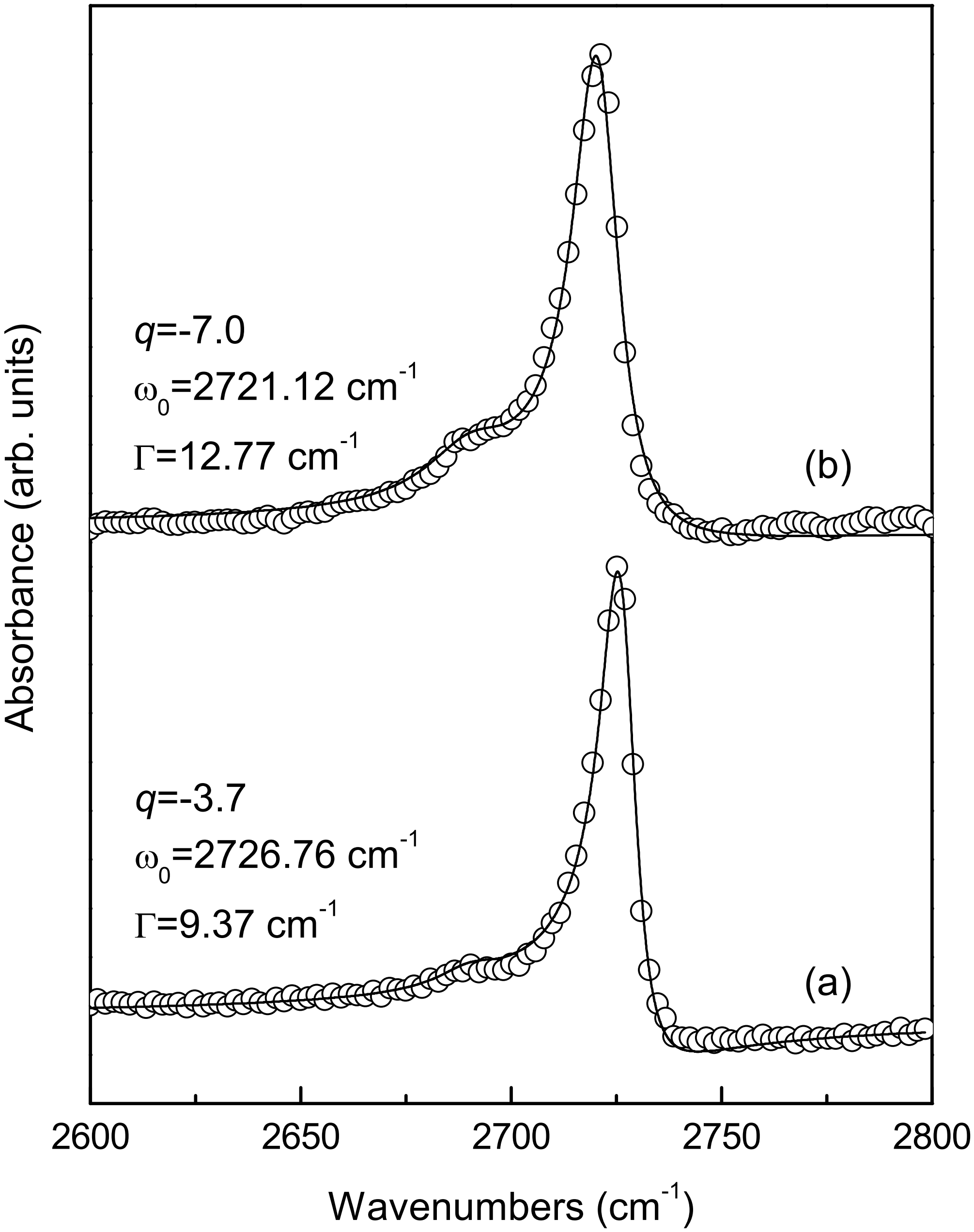

FIG. 7.6. Fano line shape fits of OD absorption peaks in (a) Mg nanorods and (b) Mg powder.

The frequency shift and shape of the vibrational spectra also depend on the thickness and surface morphology of the metal films [13]. The different morphology between nanorods and powder samples may cause slight variations in the resonance frequency and width of the absorption peaks.

The XRD pattern of Mg powder after reaction of water is shown in Fig. 7.7. From the spectrum, it can be seen that all diffraction peaks indicate only the magnesium structure. The lack of a $Mg(OH)_2$ structure provides evidence that the hydroxide forms only a thin layer over the magnesium surfaces, and their quantity is under the detection limit of XRD. Hence, similar to adsorbate molecules, the vibrations of molecules from such a thin layer couple with continuum states.

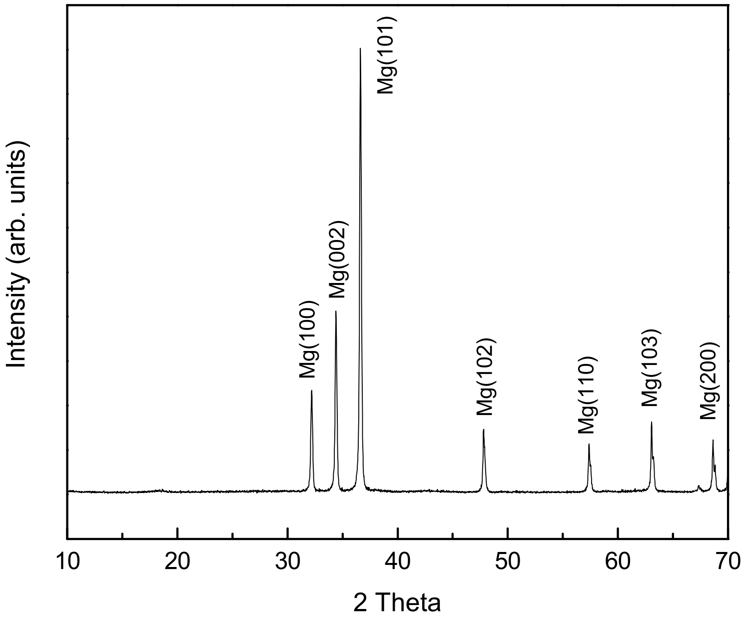

FIG. 7.7. XRD pattern of Mg powder after reaction with water.

7.5 Conclusions

In conclusion, the coupling between vibrations of hydroxide molecules and continuum electronic states from metallic magnesium results in an asymmetric Fano line shape in absorption peaks, as observed with IR absorption spectroscopy. For the insulator MgH_2, the symmetric Gaussian absorption line shape was observed. The XRD pattern suggests that a thin hydroxide layer forms on the metallic surfaces. The OH (or OD) molecules are in close proximity to the metallic continuum and hence show significant coupling.

References

[1] U. Fano, Phys. Rev. **124**, 1866 (1961).

[2] J.-P. Connerad, *Highly Excited Atoms*(Cambridge Uniersity Press, 1998).

[3] O. Krauth, G. Fahsold, N. Magg, and A. Pucci, J. Chem. Phys. **113**, 6330 (2000).

[4] J. W. Ager III, W. Walukiewicz, M. McCluskey, M. A. Plano, and M. I. Landstrass, Appl. Phys. Lett. **66**, 616 (1995).

[5] N. H. Nickel, P. Lengsfeld, and I. Sieber, Phys. Rev. B **61**, 15558 (2000)

[6] R. E. Prichard, B. R. Davidson, R. C. Newman, T. J. Bullought, T. B. Joyce, R. Jones, and S. Oberg, Semicond. Sci. Technol. **9**, 140 (1994).

[7] M. Stavola, S. J. Pearton, J. Lopata, and W. C. Dautremont-Smith, Phys. Rev. B **37**, 8313 (1988).

[8] Y. P. He, J. X. Fu, Y. Zhang, Y. P. Zhao, L. J. Zhang, A. L. Xia, J. W. Cai, Small, **3**, 153 (2007).

[9] E.F. de Oliveira, Y. Hase, Vibrational Spectroscopy **25**, 53 (2001).

[10] J. Isidorsson, I. A. M. E. Giebels, H. Arwin, and R. Griessen. Phys. Rev. B **68**, 115112 (2003).

[11] M. J. van Setten, V. A. Popa, G. A. de Wijs, and G. Brocks, Phys. Rev. B **75**, 035204 (2007).

[12] J. Li, Q. Chen, and S. Sun, Electrochimica Acta **52**, 5725 (2007).

[13] O. Krauth, G. Fahsold, A. Pucci-Lehmann, J. Molecular Structure, 482-483, 237 (1999).

APPENDIX A

Vibrations of linear tri-atomic molecules

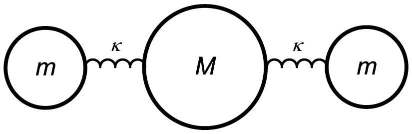

FIG. A.1. Linear tri-atomic molecule.

Consider a linear tri-atomic molecule as shown in the Fig. A.1. We can write the equations of motion as:

$$\begin{aligned} m\frac{d^2x_1}{dt^2} + \kappa(x_2 - x_1) = 0, \\ M\frac{d^2x_2}{dt^2} + \kappa(2x_2 - x_1 - x_3) = 0, \\ m\frac{d^2x_3}{dt^2} + \kappa(x_3 - x_2) = 0. \end{aligned} \tag{A.1}$$

Using the trial solution

$$x_i = x_i^0 \exp(i\omega t), \tag{A.2}$$

$$\frac{d^2x_i}{dt^2} = -\omega^2 x_i. \tag{A.3}$$

By substituting Eq. A-3 into Eq. A-1, we obtained

$$\begin{aligned}(\kappa - m\omega^2)x_1 - \kappa x_2 = 0,\\ -\kappa x_1 + (2\kappa - M\omega^2)x_2 - \kappa x_3 = 0,\\ -\kappa x_2 + (\kappa - m\omega^2)x_3 = 0.\end{aligned} \tag{A.4}$$

The homogeneous linear equations can be solved by a determinant:

$$\begin{pmatrix} \kappa - m\omega^2 & -\kappa & 0 \\ -\kappa & 2\kappa - M\omega^2 & -\kappa \\ 0 & -\kappa & \kappa - m\omega^2 \end{pmatrix} = 0. \tag{A.5}$$

Ths solution leads to

$$\omega^2(\kappa - m\omega^2)(Mm\omega^2 - \kappa M - 2\kappa m) = 0. \tag{A.6}$$

Thus,

$$\omega_1 = 0, \tag{A.7}$$

$$\omega_2 = \sqrt{\frac{\kappa}{m}}, \tag{A.8}$$

$$\omega_3 = \sqrt{\kappa\left(\frac{2}{M} + \frac{1}{m}\right)}. \tag{A.9}$$

APPENDIX B

MOCVD growth ZnO thin films.

This work is an initial part of an ongoing project (EMSL proposal No. 22290) at Pacific Northwest National Laboratory. Since the work is still in an initial stage, the recent results are included in this dissertation as an appendix.

A wide variety of thin film growth techniques have been utilized to grow oriented or epitaxial ZnO thin films [1]. Metal organic chemical vapor deposition (MOCVD) has been one of the popular techniques to grow ZnO due to its high throwing power, scalability in operation and high purity of the precursor solutions. The MOCVD system (Fig, B.1) uses metal organic compounds as precursors. The carrier gas is injected into the liquid to transfer the precursors into higher temperature zone evaporator and growth chamber. The precursors are then thermally decomposed and formed atomic layer on the substrate. The challenges for CVD precursor volatility can be tackled by using appropriately designed main and dopant precursors which decompose at similar temperatures. Precursor such as Bis(2,2,6,6-tetramethyl-3,5-heptanedionato)Zinc [$Zn(TMHD)_2$] provides a good compromise between appropriate volatility and environmental friendliness with less carbon contamination in the films [2].

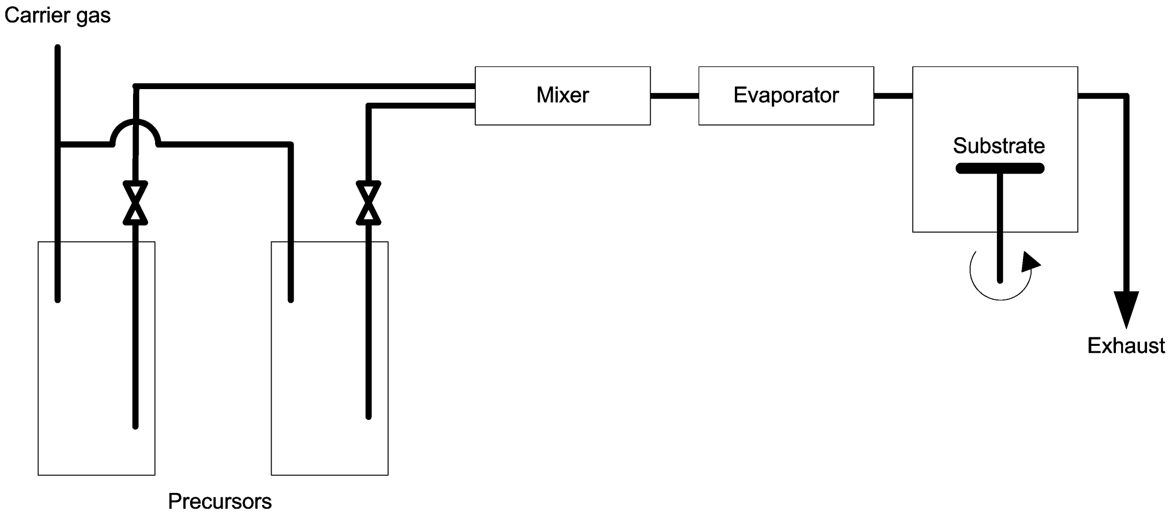

FIG. B.1. Schematic diagram of MOCVD system.

B1. Experimental

A cold-wall Emcore MOCVD system at Environmental Molecular Sciences Laboratory, PNNL was used to grow the ZnO thin-films. The zinc [$Zn(TMHD)_2$] and manganese [$Mn(TMHD)_2$] precursors were dissolved in tetrahydrofuran (THF) solution to a molar concentration of 0.025 M. The depositions were made on *c*-plane sapphire and silicon (100) oriented substrates. The Mn concentrations were varied by adjusting Zn and Mn precursors flow rate during the deposition. Visually a more yellowish color appearance was observed in the films with higher Mn contents. The nitrogen was used as carrier gas. For better oxidation, oxygen gas was also injected into reactor. We note that the thickness of ZnO films has a linear relationship with partial deposition pressure in the range of 5-60 Torr. This situation is typically present when a feed rate limited condition during the deposition exists. We also note that changing the precursor flow rates in the range of 50-100 g/hr does not significantly alter the film

TABLE B.1. Growth parameters for un-doped and ZnO:Mn films.

Substrate temperature °C	450
Vaporization temperature °C	245
Substrate roatation (rpm)	300
Vapor pressure (Torr)	60
Oxygen flow rate (sccm)	400
Argon flow rate (sccm)	2000
Nitrogen flow rate (sccm)	100
$Zn(TMHD)_2$ flow rate (g/min)	50
$Mn(TMHD)_2$ flow rate (g/min)	5-20
Depositing time (min)	20
Growth rate (Å/s)	~ 1

thickness at a given constant pressure. Deposition at vapor pressure 60 Torr results a growth rate about 1 Å/s. Details of growth parameters are presented in Table B.1.

The structural properties of the films were determined by x-ray diffraction (XRD) using Cu K_α x-ray. Elemental quantification was made by PIXE. Rutherford back scattering spectrometry (RBS) measurements were made by using 2.0 MeV He^+ ions at normal incidence. Thickness and chemical composition of the films were determined by fitting the experimental data using SIMNRA program. Furthermore, the chemical compositions were also examined with XPS, and the measurements were made by using a Physical Electronics Quantum 2000 Scanning ESCA Microprobe with monochromatic Al K_α x-rays (1486.7 eV) source and a spherical section analyzer. To remove carbon contamination at the surface, Ar^+ ion sputtering was performed using 2kV Ar^+ ions with a sputter rate of 2.8 nm/min. The etched thicknesses of the films were varied from 0.07 nm to 1.1 nm. The charge correction was made by referencing O1s line at 530.4 eV from known ZnO reference. Temperature dependent electrical conductivity measurements were made in standard 4-probe van der Pauw geometry. The films grown on single crystal sapphire substrates were used for electrical conductivity measurements.

B2. Results and discussion

The XRD spectra of undoped and Mn doped films grown on Si(100) single crystals show dominant peaks for ZnO (002) plane and (004) plane (Fig. B.2). The results confirm that the films are well-oriented along the c-axis. Within XRD detection limit, no secondary phase formation related to Mn-O is detected. The as-recorded c-axis lattice parameter for undoped sample was 5.20 Å. After assuming that the films are completely relaxed due to its 100 nm thickness and expected defects in it, the c-axis lattice parameters for Mn doping of ∼1.5 atom % and 4.5 atom % ZnO films are observed to be slightly increased to 5.21 and 5.22 , respectively. This shift to lower angle as a function of Mn incorporation is shown as an inset of Figure 1. Hence, the possible substitution of Mn^{2+} for Zn^{2+} expands the lattice parameter due to the larger ionic radius of Mn^{2+} ion. In addition, the lack of major structural disorder in doped films was confirmed by the consistency of peak widths without further broadening. A similar increase in the ZnO lattice parameter with addition of Mn was also noticed by Chikoidze *et al.* [3,4]

PIXE is highly sensitive to elemental analysis and thus is an excellent technique to quantify the overall concentration of host as well as dopant materials. A typical PIXE spectrum for the 3% atom %. Mn doped films grown on Si (100) a single

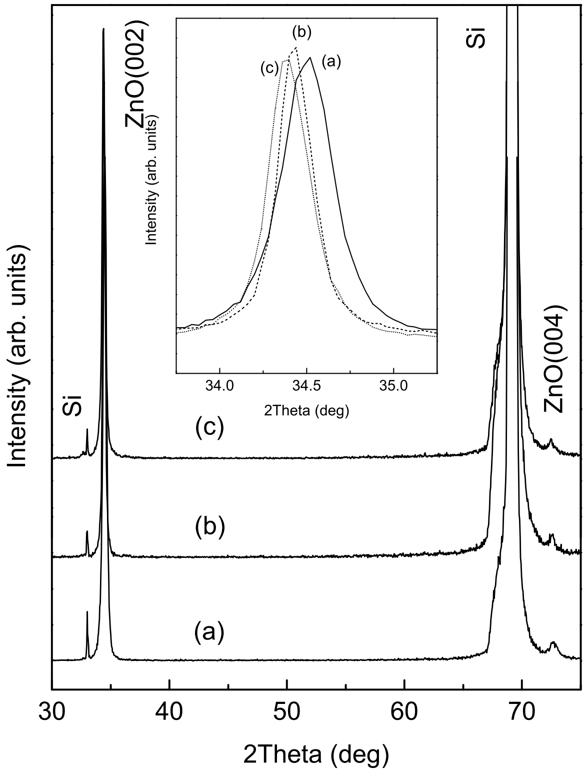

FIG. B.2. XRD diffraction patterns of ZnO films. (a) Undoped ZnO, (b) 1.5 At. % Mn, (c) 4.5 At. % Mn. Inset: Magnified ZnO (002) scan detecting slight shift in 2θ positions.

crystal is shown in Fig. B.3. The Mn K_α emission along with Zn and Si peaks, can be clearly seen in the spectrum. The inset of Fig. B.3 represents RBS spectra of the same Mn:ZnO film grown on a Si (100) single crystal. The overall uniformity in the Mn distribution can be realized in the spectrum. We also use these data for the calculation of film thickness 100 nm. From the curve profile, no noticeable diffusion of the film into the substrate is observed. High resolution XPS spectra for the regions of Zn 2p, O 1s, Mn 2p and Mn 3p are shown in Figs. B.4 and B.5. The intensity ratios between O to Zn were mostly un-affected by Mn incorporation. Despite the lack of Mn dopant in undoped ZnO sample, there is a weak and broad peak exhibits at an energy around 640 eV, which is Auger (AES) line of Zn 2p state (Fig. B.5) originating from Auger emission of Zn atoms. Hence, instead of using Mn 2p peak, we used weaker Mn 3p peak for the analysis of Mn composition, so that we can avoid the convolution of Zn Auger emission. The Mn 2p and Mn 3p peak positions and widths are consistent for all Mn contents which indicate that Mn^{2+} state is dominant in all doped films.

The ratio of zinc to oxygen compositions as a function of Mn content calculated from both XPS and PIXE are presented in Fig. B.6. The data are presented in four different sets as (a) from PIXE technique, (b) As recorded XPS surface scan, (c) After Ar+ ion sputtering in XPS and (d) XPS corrected atomic concentration, respectively. One of the major reasons for presenting the data in such a way is to discuss the role of surface carbon, and hydrocarbons in XPS technique, adjusting it with correction and comparing with independent PIXE technique. As shown in Fig, 5(b), by calculating the ratio of Zn to O peaks in as-recorded sample, we have seen significant variation in

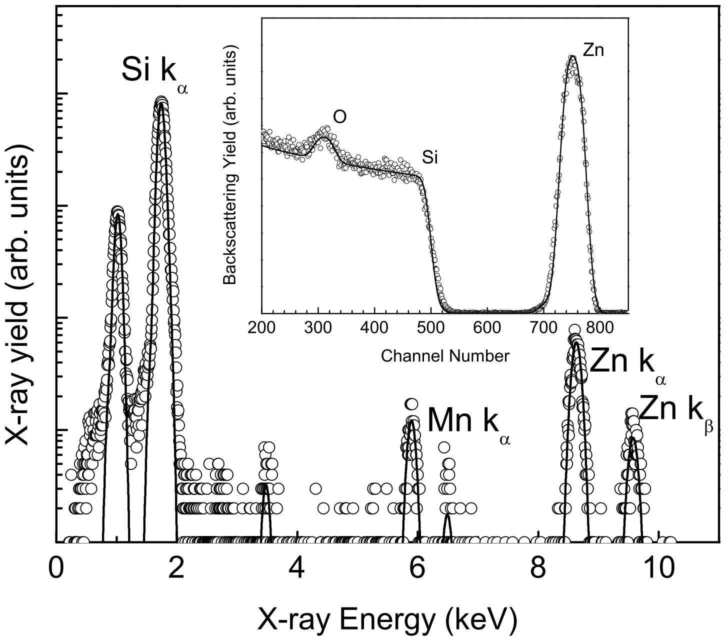

FIG. B.3. PIXE spectrum of ZnO:Mn (4.5 At. % Mn) sample. RBS spectrum is shown in inset. The solid lines represent the modeled spectra.

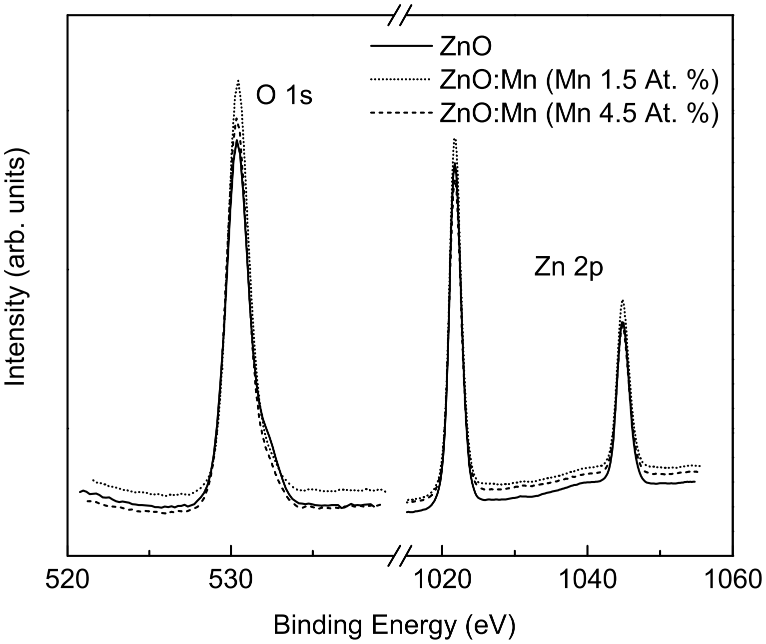

FIG. B.4. XPS spectra for ZnO and ZnO:Mn films. Zn and O regions.

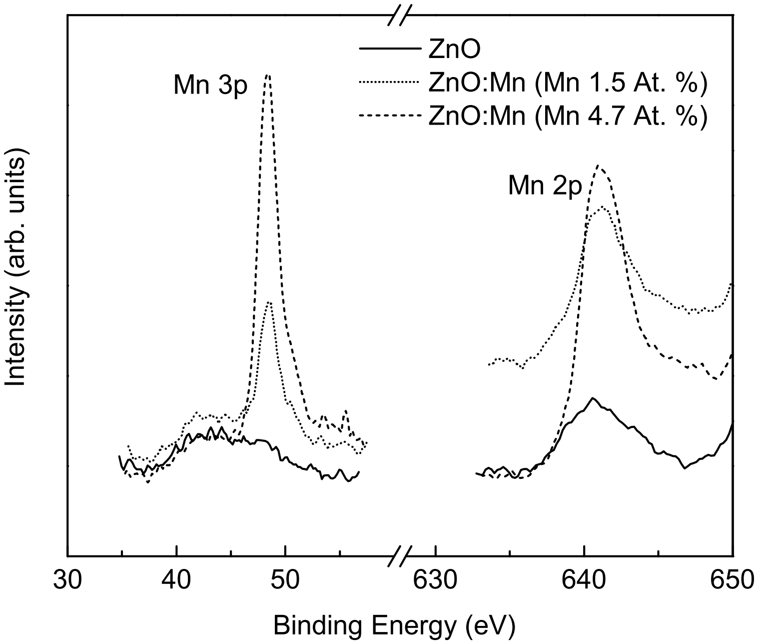

FIG. B.5. XPS spectra for ZnO and ZnO:Mn films. Mn regions.

it with Mn addition. By considering the peaks for surface hydrocarbons and correcting it in the total, we have seen that variation in the Zn to O peak ratio was somewhat reduced. Ar^+ ion sputtering was used to remove surface layers and XPS analysis after sputtering indicates substantial removal of the surface hydrocarbons. As seen in Fig. 5(d), the variation in Zn to O peak ratio as a function of Mn addition narrowed considerably as a result of cleaning of surface contaminants and hydrocarbons. For most part, the XPS ratio analysis indicates Zn rich films. Some of the major reasons for it can be oxygen sensitivity factor is different than Zn sensitivity factor. Also as noted previously oxygen is known to sputter out preferentially [5]. However, even though not detected in our analysis, we can not completely rule out minor percentage of sub-stoichometric ZnO. As seen in Fig. B.6a, after comparing the data with completely independent and sensitive PIXE technique, we have seen that the ratio of Zn to O gradually decreases from near 1 as a function of Mn doping concentration in ZnO films, which should be an expected outcome. We would like to also note that the slight differences in Mn atomic concentrations calculated by PIXE and XPS techniques are due to differences in the sensitivity factors, usage of 3p line instead of 2p line, and normalization process during calculations in the case of XPS analysis.

The temperature dependent conductivity results indicate that conductivity decreases with increasing Mn content in ZnO (Fig. B.7). The results are in good agreement with other reports of Mn doped ZnO [6,7]. By using the relationship between conductivity of semiconductor as a function of temperature [$\sigma \propto \exp(-\Delta E/kT)$], the trends for all films are more or less similar. The estimated activation energy for all

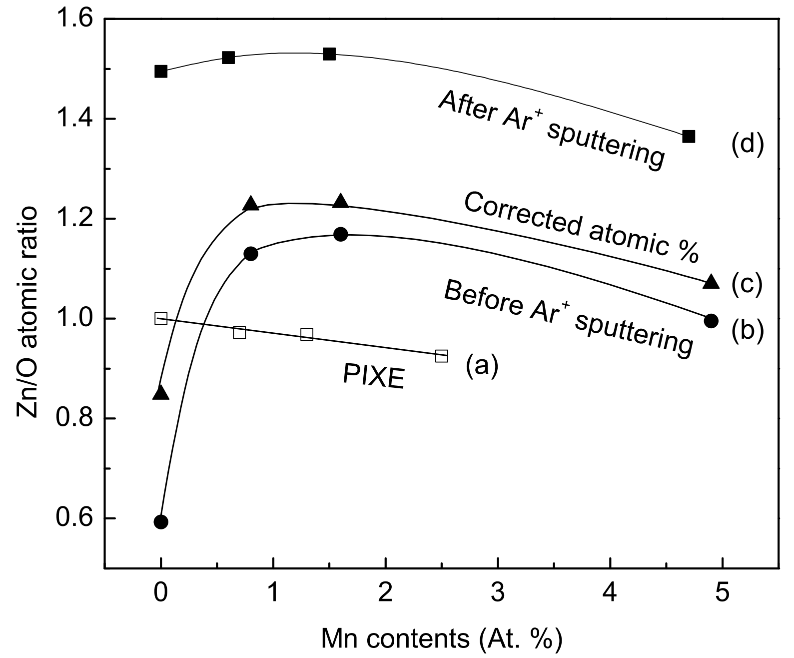

FIG. B.6. The ratio of zinc to oxygen compositions as a function of Mn content calculated from both XPS and PIXE. (a) from PIXE technique, (b) As recorded XPS surface scan, (c) After Ar^+ ion sputtering in XPS and (d) XPS corrected atomic concentration.

films lies between 0.04 to 0.05 eV. However, the Arrhenius plots in Fig. B.7 do not produce perfect straight lines, because we have neglected the temperature dependence of electron mobility, and possibly association of different defects states in the films. These results also support Zn rich films observed in XPS analysis. Similar characteristic trends between undoped and Mn doped films suggest that Mn acts neither donor nor acceptor in ZnO, and only native defects contribute to the free carriers. It is not surprising, since the Mn^{2+} state lies within the valence band [8], thereby Mn impurities do not generate additional free carriers. Look *et al.* [9] suggest that zinc interstitial Zn_i is most likely to be native shallow donor and experimental results also confirm that the defect level lie 0.03-0.04 eV below conduction band [10], and from XPS analysis defects in our films are presumably dominated by zinc interstitials. The possibility for increasing resisitivity with Mn content is due to native defects in ZnO, such as Zn_i were suppressed by Mn doping. With the help of photoluminescence spectroscopy, the reduction of native defects by Mn doping was also reported by Philipose *et al.* [11] by observing a strong suppressing of midgap emission that originates from native defects.

B3. Summary

In summary, we have tried to correlate the ion beam and surface properties of Mn doped ZnO films with observation of suppressed conductivity in ZnO. The films were well oriented in *c*-axis direction with wurtzite structure. Within our detection limit we have not seen any secondary phases which are not surprising by considering

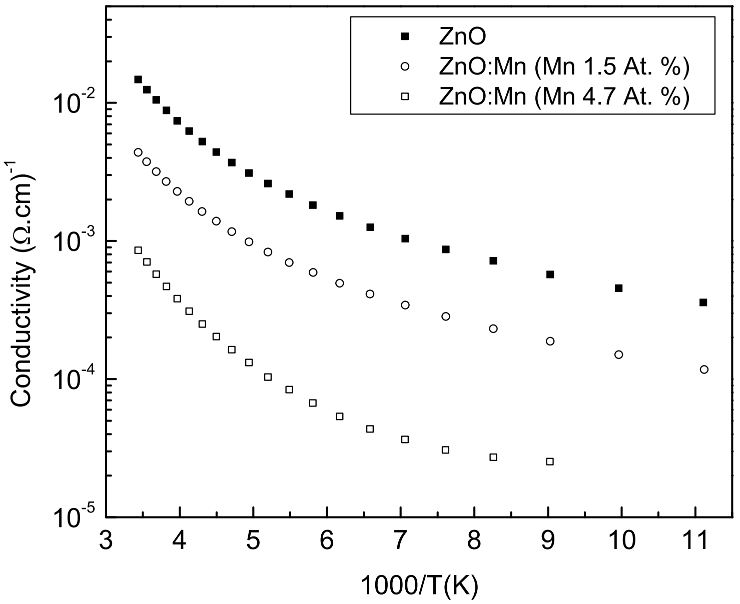

FIG. B.7. Temperature dependent electrical conductivity for undoped as well as ZnO:Mn films.

relatively low Mn doping concentration. The RBS measurements also confirm uniform distribution of Mn dopants throughout the film. Electrical conductivity results prove the conductivity suppressing nature of Mn^{2+} ions in ZnO host. The XPS results show that Mn^{2+} state is most likely to be dominant state. Thus, impact of Mn impurities on native ZnO defect concentrations plays the major role in defining electrical properties of ZnO.

References

[1] R. Triboulet, and J. Perriere, Progress in Crystal Growth and Characterization of Materials, **47**, 65 (2003).

[2] L.V. Saraf, M. H. Engelhard, C. M. Wang, A. S. Lea, D. E. McCready, V. Shutthanandan, D. R. Baer and S. A. Chambers, J. Materials Res. **22**, 1230 (2007).

[3] E. Chikoidze Y. Dumont F. Jomard, D. Ballutaud, P. Galtier, and O. Gorochov, and D. Ferrand, J. Appl. Phys. **97**, 10D327 (2005).

[4] E. Chikoidze, Y. Dumont, H.J. von Bardeleben, J. Gleize, F. Jomard, E. Rzepka, G. Berrerar, D. Ferrand and O. Gorochov, Appl. Phys. A **88**, 167 (2007).

[5] R. Kelly, Surf. Sci., **100**, 85 (1980).

[6] J. Han, M. Shen, W. Cao, A.M.R. Senos and P.Q. Mantas, Appl. Phys Lett. **82**, 67 (2003).

[7] W. Chen, J. Wang and M. Wang, Vacuum **81**, 894 (2007).

[8] K. R. Kittilstved, W. K. Liu and D. R. Gamelin, Nature Materials **5**, 291 (2006).

[9] D. C. Look , J. W. Hemsky and J. R. Sizelove, Phys. Rev. Lett. **82**, 2552(1999).

[10] D. G. Thomas, J. Phys. Chem. Solids, **3**, 229 (1957).

[11] U. Philipose, S. V. Nair, S. Trudel, C. F. de Souza S. Aouba, R. H. Hill and H. E. Ruda, Appl. Phys. Lett. **88**, 263101 (2006).

LIST OF PUBLICATIONS

- W. M. Hlaing Oo, M. D. McCluskey, J. Huso, and L. Bergman, "Infrared and Raman spectroscopy of ZnO nanoparticles annealed in hydrogen." *J. Appl. Phys.* **102**, 043529 (2007).

- M. D. McCluskey, S. J. Jokela, and W. M. Hlaing Oo, "Hydrogen in bulk and nanoscale ZnO." *Physica:B* **376-377**, 690 (2006).

- M. A. Scarpulla, B. L. Cardozo, R. Farshchi, W. M. Hlaing Oo, M. D. McCluskey, K. M. Yu, and O. D. Dubon, "Ferromagnetism in $Ga_{1-x}Mn_xP$: evidence for inter-Mn exchange mediated by localized holes within a detached impurity band." *Phys. Rev. Lett.* **95**, 207204 (2005).

- W. M. Hlaing Oo, M. D. McCluskey, A. D. Lalonde, and M. G. Norton, "Infrared spectroscopy of ZnO nanoparticles containing CO_2 impurities." *Appl. Phys. Lett.* **86**, 073111 (2005).